SHADOW DETECTION ON MULTISPECTRAL IMAGES

A THESIS SUBMITTED TO
THE GRADUATE SCHOOL OF NATURAL AND APPLIED SCIENCES
OF
MIDDLE EAST TECHNICAL UNIVERSITY

BY

HAZAN DAĞLAYAN SEVİM

IN PARTIAL FULFILLMENT OF THE REQUIREMENTS
FOR
THE DEGREE OF MASTER OF SCIENCE
IN
INFORMATION SYSTEMS

SEPTEMBER 2015

Approval of the thesis:

SHADOW DETECTION ON MULTISPECTRAL IMAGES

submitted by **HAZAN DAĞLAYAN SEVİM** in partial fulfillment of the requirements for the degree of **Master of Science in Information Systems Department, Middle East Technical University** by,

Prof. Dr. Nazife Baykal _____
Dean, Graduate School of **Informatics**

Prof. Dr. Yasemin Yardımcı Çetin _____
Head of Department, **Information Systems**

Prof. Dr. Yasemin Yardımcı Çetin _____
Supervisor, **Information Systems, METU**

Examining Committee Members:

Assoc. Prof. Dr. Altan Koçyiğit
Information Systems, METU _____

Prof. Dr. Yasemin Yardımcı Çetin
Information Systems, METU _____

Assist. Prof. Dr. Ersin Karaman
MIS Department, Atatürk University _____

Assoc. Prof. Dr. Banu Günel Kılıç
Information Systems, METU _____

Assoc. Prof. Dr. Alptekin Temizel
Modeling and Simulation, METU _____

Date: _____

I hereby declare that all information in this document has been obtained and presented in accordance with academic rules and ethical conduct. I also declare that, as required by these rules and conduct, I have fully cited and referenced all material and results that are not original to this work.

Name, Last Name: HAZAN DAĞLAYAN SEVİM

Signature :

ABSTRACT

SHADOW DETECTION ON MULTISPECTRAL IMAGES

DAĞLAYAN SEVİM, HAZAN
M.S., Department of Information Systems
Supervisor : Prof. Dr. Yasemin Yardımcı Çetin

September 2015, 93 pages

Shadows caused by clouds, mountains or high human-made structures pose challenges for identification of objects from satellite or aerial images since they deteriorate and mask true spectral properties of the objects. Therefore, they should be detected to accurately classify objects. Moreover, in change detection problems, shadows deteriorate performance because mere spectral changes act as actual object changes. Shadows are also useful as cues for estimating the height of an object or determining the time of recording. This study is dedicated to developing novel algorithms for detecting shadows on multispectral images using different color spaces. The proposed methods are compared with the methods in the literature.

Keywords: remote sensing, shadow detection, multispectral, aerial images, Worldview-2

ÖZ

ÇOK BANTLI İMGELERDE GÖLGE TESPİTİ

DAĞLAYAN SEVİM, HAZAN
Yüksek Lisans, Bilişim Sistemleri Bölümü
Tez Yöneticisi : Prof. Dr. Yasemin Yardımcı Çetin

Eylül 2015 , 93 sayfa

Bulutlar, dağlar veya insan yapımı yüksek yapıların sebep olduğu gölgeler, objelerin gerçek spectral özelliklerini bozduğu ve gizlediği için uzaydan ya da havadan görüntülenen objelerin tanımlanmasında engel oluşturuyor. Bu yüzden, objeleri doğru bir şekilde sınıflandırabilmek için gölgeler tespit edilmelidir. Diğer bir taraftan değişiklik tespiti problemlerinde sadece spektral değişiklikleri gerçek obje değişimi olarak görüldüğünden gölgeler performansı kötüleştirir. Gölgeler ayrıca objenin yüksekliğini tahmin etmede veya kaydın alındığı zamanı belirlemede ipucu olarak kullanılır. Bu çalışma çok bantlı imgelerdeki gölgeleri, farklı renk uzayları kullanarak tespit etmek için yeni algoritmalar geliştirmeye adanmaktadır. Önerilen metotlar literatürdeki metotlarla karşılaştırılır.

Anahtar Kelimeler: uzaktan algılama, golge tespiti, multispektral, havadan imgeler, Worldview-2

to ones who aren't imprisoned in shadow but drink sun

ACKNOWLEDGMENTS

I would like to express my grateful and also my respect to my thesis advisor Prof. Dr. Yasemin Yardımcı Çetin for her guidence and valuable suggestions in every step of my study. She has always encouraged me to work harder.

I thank my dear friend Didem Özışık Başkurt for her support and comments. She has succored whenever I need her help both technical and psychological support. Also, I am thankful to Fatih Ömrüuzun for his valuable advices.

I also would like to thank my workmates from Atilim University for their support. Especially, I am grateful to Damla Topallı who always helps me when I am in trouble.

A special word of thanks is for my friends for making this process smooth and joyful. Especially, Fatma Özkaya who succors when I had a problem with English at midnight and Mehmet İmir who always encouraged and helped me deserve my special thanks.

I also would like to thank my family because I always feel their support. They always argue that a girl must study so I never gave up studying. I couldn't manage all this if they weren't farsighted people. Moreover, thanks to my husband's family for their interest and cooking. They satisfied our need when we study.

Finally, I would like to express my deepest gratitude to my husband Emre Sevim for his love and support. This thesis would not have been written unless he had come to library and taken a coffee break with me.

TABLE OF CONTENTS

LIST OF TABLES

LIST OF FIGURES

LIST OF ABBREVIATIONS

ALS	Airborne Laser Scanner
DSM	Digital Surface Model
FN	False Negative
FP	False Positive
HCV	Hue-Chroma-Value
HSI	Hue-Saturation-Intensity
HSV	Hue-Saturation-Value
NDVI	Normalized Difference Vegetation Index
NIR	Near Infrared
RGB	Red-Green-Blue
TN	True Negative
TP	True Positive

CHAPTER 1

INTRODUCTION

1.1 Motivation

Research on remote sensing images is one of the most popular topics of the recent years. Utilization of remote sensing is critical to realize the problem and to seek for solutions to the problems of the many areas such as urban planning [9], urban growth monitoring [28], military surveillances [26], navigation [5], [47], crop yield estimation [17], [27], disaster management [44], [29] and traffic management [31].

As a result of the increase of the volume and accessibility of remote sensing images, they have been used more often. Besides, the methods which increase the quality of the spatial resolution of the images have been improved [46], [15], [34]. This improvement further contributes to the popularity of the research area. Therefore, the advantages of detailed image analysis has been increasing gradually.

One of the crucial area of the remote sensing is shadow detection. Shadow detection can help to find solution to more than one problem. Classification of the objects in the image is a commonly dealt problem among these. In an aerial image, although that similarity of the classes and the variety of the class obstruct the image classifications is an important problem, the classification of the shadow region is a major problem for classification. Shadow modifies the radiometric information of the materials and so the materials under the shadow do not indicate their properties. Therefore, without shadow detection, accurate detection and identification of objects may not be possible. In addition, in change detection problem, when two images are compared, detection may be false because of the radiometric differences of shadow and non-shadow region. Therefore, in change detection problems, firstly shadow is detected, then algorithms works for the problem. Moreover, shadow is used as cue to infer about 3D information of the objects such as shape or its height. Consequently, shadow detection in aerial/satellite imagery is one of the challenging problems and an important research topic for remote sensing.

1.2 Scope of the Thesis

In this study, WorldView-2 images, which have high spectral resolution with 8-band including wider range on electromagnetic spectrum than standard RGB images with

3 bands, are used. The main objective of this study is to detect shadows automatically on multispectral remote sensing images. Moreover some secondary objectives are listed as follows:

- To present automatic shadow detection methods on multispectral 8-band images and to test these methods.
- To investigate the ability of the multispectral 8-band images compared to standard RGB images on shadow detection and to determine the contribution of new spectral bands..
- To select some shadow detection methods from the literature, to test these methods and to compare their results with novel proposed methods.
- To compare the success of the automatic threshold and manual threshold detection.

1.3 Outline of the Thesis

This document is organized as five chapters including introduction, background, literature, shadow detection methods, experiments and conclusion. After general information about shadow detection and remote sensing is given, the aim of the this thesis is stated in this chapter. In Chapter 2, shadow types are defined and shadow's properties and the difference between shadow and non-shadow regions is explained. Moreover, different color spaces which are used to detect shadows are provided. The shadow detection studies in the literature are presented in Chapter 3. In Chapter 4, shadow detection methods based on ratio suggested in the literature are explained in detail and by presenting justifications, novel ratios are proposed. The metrics for measuring of the success of the methods are defined in Chapter 5. Moreover, the shadow detection ratios mentioned in Chapter 4 are tested and their experimental results are compared. Finally, the research is concluded with a summary of our contributions and future works are mentioned.

CHAPTER 2

BACKGROUND

2.1 Shadows and Their Properties

2.1.1 Definition of Shadow

Shadow occurs when direct light from a source of illumination is obstructed by objects totally or partially [4], [40], [19]. Shadows are divided into two classes: self shadow and cast shadow. Self shadow occurs on the object when it is not illuminated by direct light, while cast shadow is the projection of the object on the area. There are two types of cast shadows: umbra and penumbra. Umbra forms if the light source is completely obstructed, whereas penumbra occurs if it is partially obstructed as shown in Fig.2.1.

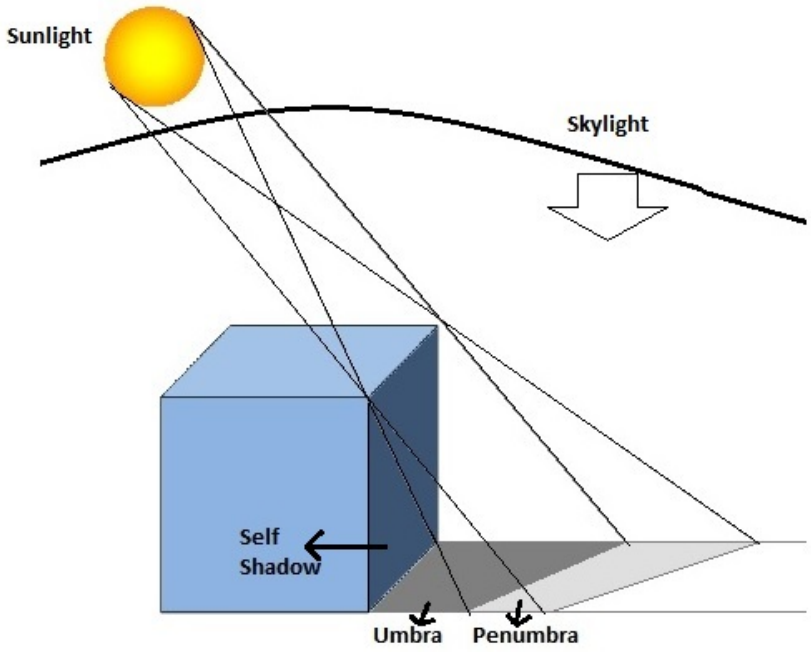

Figure 2.1: Shadow types

Arevalo et. al argues that the distinction among umbra and penumbra is not substantial as well as the self shadows on the aerial or satellite images [4]. Hence, in the

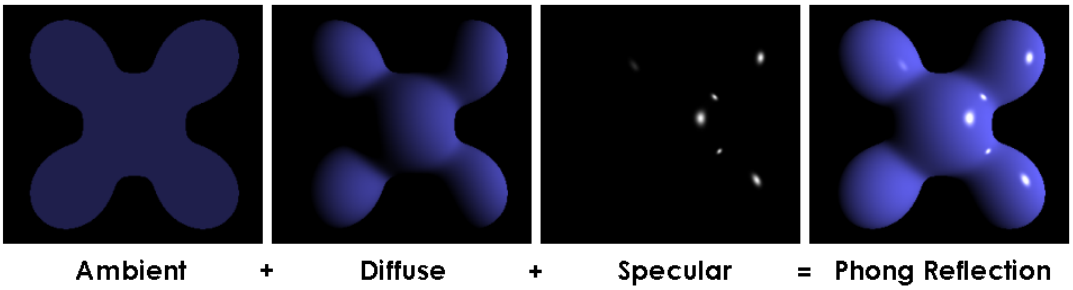

Figure 2.2: The components of the Phong Reflection Model [6]

literature most of the studies in remote sensing focus on only cast shadows. However, in this study our main assumption is that because self shadows occur on the aerial or satellite images, they are also important and should be detected.

2.1.2 Properties of Shadow

A surface either emits or reflects the light which comes from the illumination source. According to Phong Reflection Model which is an empirical model of interaction between illumination and object's surface, the light reflected from the surface consists of three types of reflection: ambient, diffuse and specular. Ambient reflection (L_a) scatters the skylight in the outdoor scene not depending on the direction so in all directions all surfaces get the light equally. The reflection changes only with the ambient reflection coefficient. Diffuse reflection (L_d) scatters the direct light reflected uniformly in all directions. Finally, specular reflection (L_s) scatters the direct light in a single direction as a mirror [14]. The effects of the light on the object is seen in Figure 2.2.

Since the direct sunlight is obstructed in a shadow area, it is illuminated by only scattered light (skylight). The reflected light at wavelength λ at a point $\vec{p}$ on the object's surface can be expressed as the sum of three terms

$$L_r(\lambda, \vec{p}) = L_a(\lambda, \vec{p}) + L_d(\lambda, \vec{p}) + L_s(\lambda, \vec{p}) \tag{2.1}$$

where $L_r(\lambda, \vec{p})$,$L_a(\lambda, \vec{p})$, $L_d(\lambda, \vec{p})$ and $L_s(\lambda, \vec{p})$ are the radiance of the light with the unit for emitted power, the ambient reflection term, the diffuse reflection term, and the specular reflection term, respectively [40]. Since the diffuse reflection term and the specular reflection term are related with the direct light and the ambient reflection term is the result of reflected light among surfaces in the environment, for shadow region, the term is reconstructed as

$$L_{r_{shadow}}(\lambda, \vec{p}) = L_a(\lambda, \vec{p}) \tag{2.2}$$

Let $E(\lambda)$ be the term representing incoming power called irradiance and $S(\lambda)$ be the sensitivity of the camera. Camera's sensor responses ρ_k are described as [14]

$$\rho_k = \int_{w_k} E(\lambda)S(\lambda)d\lambda \tag{2.3}$$

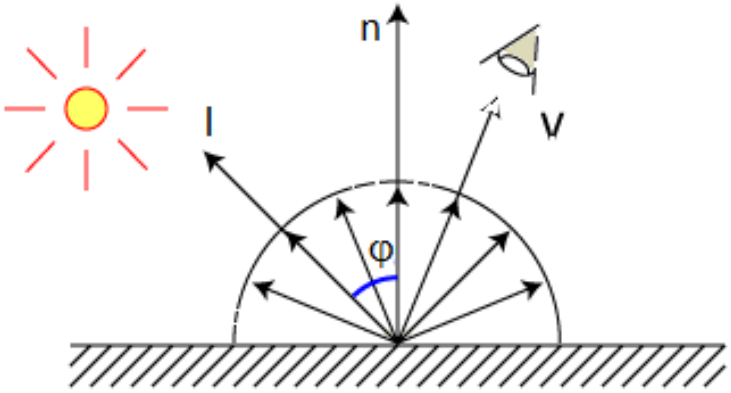

Figure 2.3: Diffuse Reflection

where k represents the red, green and blue bands and w_k is the bounded interval of the wavelength of each band. For non-shadow pixels, while α is called albedo which is the proportionality factor between irradiance and radiance, Expression (2.3) is written as [12]

$$\rho_k = \int_w \alpha(L_a(\lambda) + L_d(\lambda, \vec{p}) + L_s(\lambda, \vec{p}))S(\lambda)d\lambda \tag{2.4}$$

However, the reflected light is the only illumination of shadow region. Therefore, the other terms are omitted from the expression so that

$$\rho_{k_{shadow}} = \int_w \alpha L_a(\lambda)S(\lambda)d\lambda \tag{2.5}$$

That sensor responses are smaller values in shadow region than the responses in non-shadow region is concluded from the expressions (2.4) and (2.5).

$$\rho_{k_{shadow}} < \rho_{k_{non-shadow}} \tag{2.6}$$

As a result, the intensity I of the shadow is lower than the intensity of non-shadow region

$$I = \frac{\rho_R + \rho_G + \rho_B}{3} \tag{2.7}$$

where $k \in \{Red, Green, Blue\}$ [18]. Therefore, the shadow region is darker than the non-shadow region.

Based on the Phong reflection model mentioned above, the components of the reflection light are ambient, diffuse and specular. Ambient reflection is both in shadow and non-shadow region. Moreover, the specular reflection can be ignored for most urban areas because these images are usually matte. Therefore, the only difference reflection of shadow and non-shadow regions is the diffuse reflection shown in Fig.2.3 which can be expressed as

$$L_d(\lambda, \vec{p}) = I_d(\lambda, \vec{p}) \cos\varphi \tag{2.8}$$

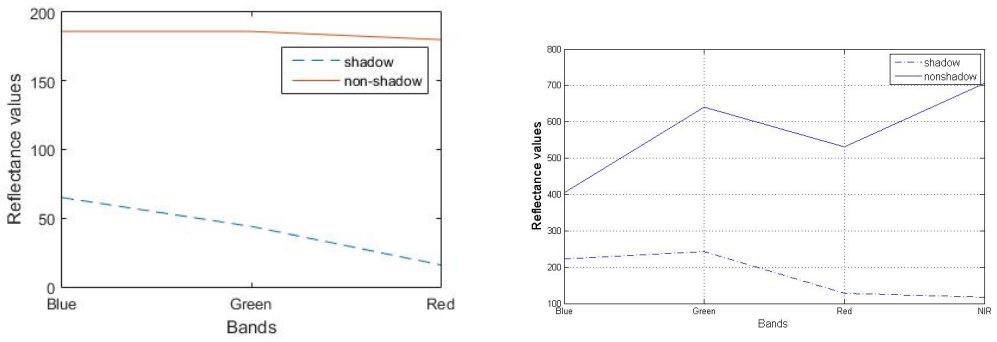

(a) (b)

Figure 2.4: (a) Reflectance values of shadow and non-shadow pixels on white surface (b) Reflectance values of shadow and non-shadow pixels on aerial image

where $I_d(\lambda, \vec{p})$ is light radiance at point $\vec{p}$ and φ is the angle between the direction of the light source (l) and the normal of the surface ($\vec{n}$). As a result, the difference intensity of shadow and non-shadow regions on red, green and blue channels, represented by ΔI_R, ΔI_G and ΔI_B can be expressed as

$$\Delta I_R = \int \alpha_R I_d(\lambda, \vec{p}) \cos\varphi S_R(\lambda) d\lambda \tag{2.9}$$

$$\Delta I_G = \int \alpha_G I_d(\lambda, \vec{p}) \cos\varphi S_G(\lambda) d\lambda \tag{2.10}$$

$$\Delta I_B = \int \alpha_B I_d(\lambda, \vec{p}) \cos\varphi S_B(\lambda) d\lambda \tag{2.11}$$

It is assumed that the parts given on 2.12 which includes light radiance and sensor sensitivities have equal values for the white light source [20].

$$\int I_d S_R(\lambda) d\lambda = \int I_d S_G(\lambda) d\lambda = \int I_d S_B(\lambda) d\lambda \tag{2.12}$$

However, since albedo α is positive proportional to the wavelength, red channel has the biggest change whereas blue channel has the smallest one [25]. Thus;

$$\Delta I_R > \Delta I_G > \Delta I_B \tag{2.13}$$

The other property of shadow is that effects of scattering increases from long to short wavelengths [1]. Therefore, the least change between shadow and non-shadow belongs to blue channel and blue is the dominant channel in shadow [3], [25]. Nevertheless, on aerial images shadows usually form on asphalt or greenish grassland so green channel has higher values than blue channel. On the other hand, because of NIR bands have long wavelengths, there is a big change between shadow and non-shadow regions on NIR bands. As a result, NIR band is more preferred to distinguish the shadow from the non-shadow region [1]. The reflectance values of shadow pixels in each bands are seen on Figure 2.4. In shadow pixels, green channel values have highest values and the maximum change between shadow and non-shadow regions is on NIR values.

In addition, shadow region maintains materials properties with the decreased values. Therefore, the material has similar spectral properties both shadow and non-shadow regions [35]. The idea is supported with the examples, in which pixels are chosen from shadow and non-shadow regions, in Fig. 2.5.

Shadow region also has higher saturation and hue values than non-shadow regions. The reason of high values are explained in Chapter 4 in detail after the definitions of hue and saturation are given.

2.2 Color Spaces

While the objects and surfaces absorb a portion of the incident light, they reflect remaining part. The color is the light which people and animals perceive from the objects [22]. It is concluded from the argument that our eyes can not sense all wavelengths. Figure 2.6 shows a graph of the electromagnetic spectrum and the range, which humans can observe, with respect to their wavelength. The color, which we perceive, is the result of the mixture of light of different wavelengths in the visible spectrum [22]. Red, green and blue are in the range which people can perceive. RGB is a widely used color space which consists of red, green and blue color components. The wavelengths of red, green and blue have a wider range when RGB is compared with the other three-channel combinations [30]. However, it does not mean that red, green and blue obtain all tones of color; some tones can not be obtained by any combinations of these three channels [22]. Therefore, we also observe the change of shadow in other color spaces.

2.2.1 RGB

RGB color space consists of three primary colors which are Red, Green and Blue bands. It is a unit cube as shown in Fig. 2.8. The amounts of Red, Green and Blue determine the color. For example, while the value (1,0,1) represents the Magenta secondary color, an equal amount of R, G and B represents the gray levels.

2.2.2 HSI

Hue is defined as a color attribute that describes a pure color (pure yellow, orange or red), saturation describes how much a pure color is diluted with white light [22]. Moreover, the chromaticity is defined as togetherness of hue and saturation. Since the brightness is a subjective term and it can not be measured, the intensity, which is the amplitude of the pixel is used on the third dimension [22].

HSI color space consists of Hue, Saturation and Intensity and is transformed from the

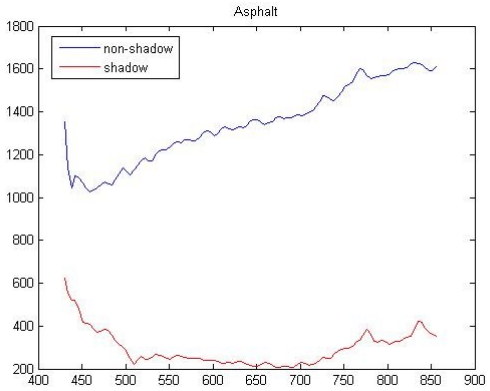

(a)

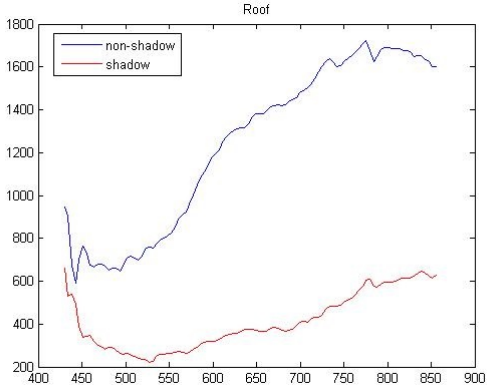

(b)

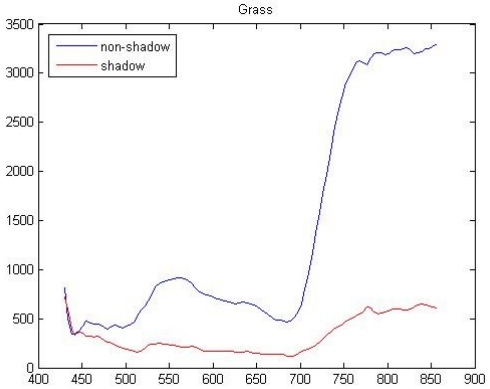

(c)

Figure 2.5: (a) Asphalt on shadow and non-shadow (b) Roof on shadow and non-shadow (c) Grass on shadow and non-shadow

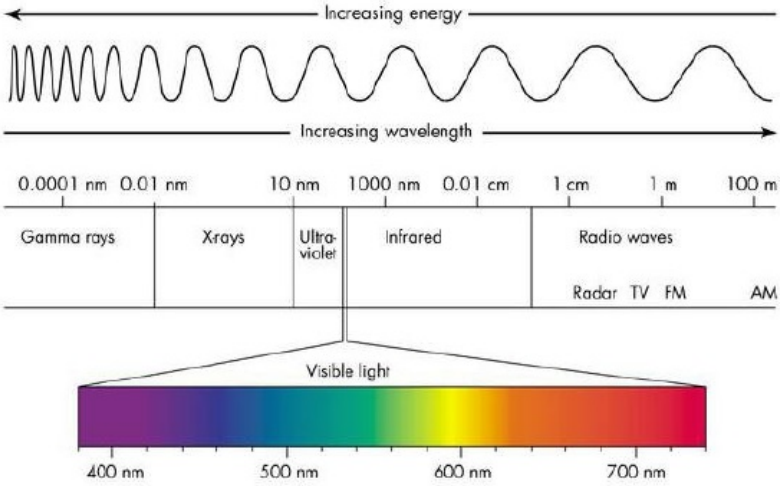

Figure 2.6: Electromagnetic Spectrum

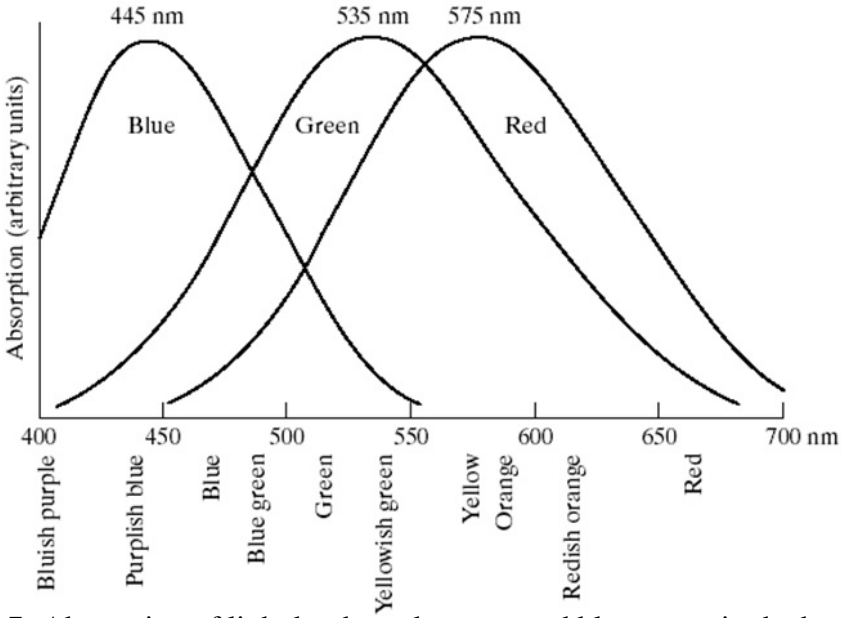

Figure 2.7: Absorption of light by the red, green, and blue cones in the human eye as a function of wavelength [22]

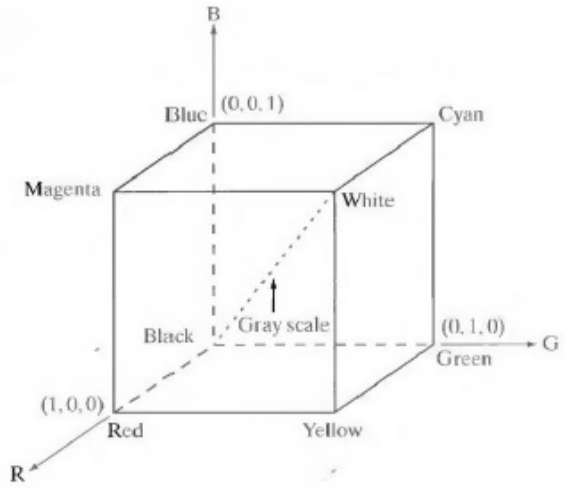

Figure 2.8: RGB Color Cube

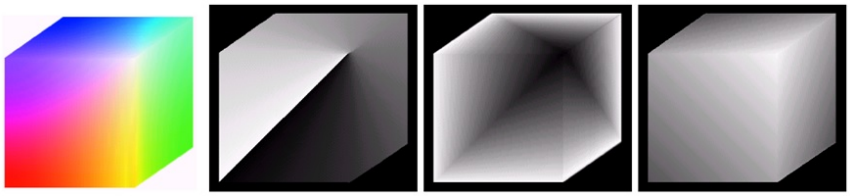

Figure 2.9: a) RGB Color Cube, b) Hue of (a), c) Saturation of (a), d) Intensity of (a)

RGB model as [38]

$$\begin{bmatrix} I \\ V_1 \\ V_2 \end{bmatrix} = \begin{bmatrix} \frac{1}{3} & \frac{1}{3} & \frac{1}{3} \\ \frac{-\sqrt{6}}{6} & \frac{-\sqrt{6}}{6} & \frac{\sqrt{6}}{3} \\ \frac{1}{\sqrt{6}} & \frac{-2}{\sqrt{6}} & 0 \end{bmatrix} \begin{bmatrix} R \\ G \\ B \end{bmatrix} \tag{2.14}$$

$$S = \sqrt{V_1{}^2 + V_2{}^2} \tag{2.15}$$

$$H = \arctan \frac{V_2}{V_1} \tag{2.16}$$

if $V_1 \neq 0$, otherwise H is undefined.

2.2.3 HSV

HSV color space is similar to HSI. It consists of Hue, Saturation and Value. The triangle based model of HSV can be transformed from RGB model as

$$V = \frac{R + G + B}{3} \tag{2.17}$$

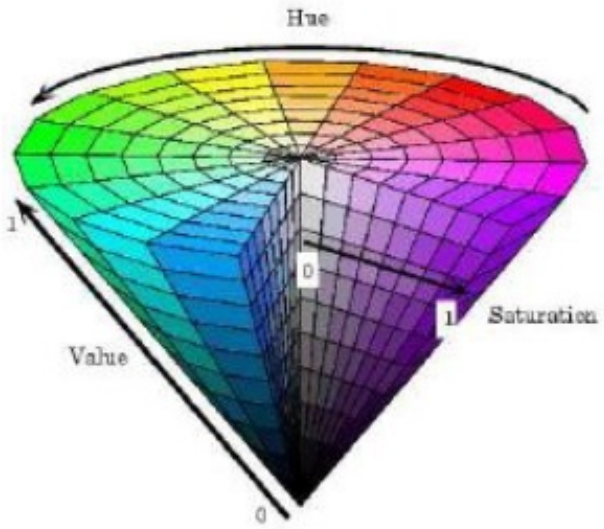

Figure 2.10: Hue, Saturation and Value

$$S = 1 - \frac{3}{R+G+B} min(R,G,B) \tag{2.18}$$

$$H = \begin{cases} \theta & \text{if } B \leq G \\ 360^\circ & \text{if } B > G \end{cases} \tag{2.19}$$

in which

$$\theta = \arccos\{\frac{\frac{1}{2}[(R-G)+(R-B)]}{\sqrt{(R-G)^2+(R-B)(G-B)}}\} \tag{2.20}$$

Hue is the angle from the red axis, while saturation is the length of the vector. It can be seen in Fig 2.10

2.2.4 HCV

The components of HCV space is hue, chroma and value, respectively. It is a way of separation the achromatic component, which means that the light that has equal components such as gray, black, white, value is reflected, and chromatic component, which has some dominant values such as blue, green, hue, chroma [24]. The relation of HCV space with RGB given as

$$V = \frac{R+G+B}{3} \tag{2.21}$$

$$H = tan^{-}1(\frac{R-B}{\sqrt{3}(V-G)}) \tag{2.22}$$

$$C = \begin{cases} \frac{V-G}{\cos H} & \text{if } |\cos H| \leq 0.2 \\ \frac{R-B}{\sqrt{3}\sin H} & \text{if } |\cos H| > 0.2 \end{cases} \tag{2.23}$$

2.2.5 Luminance and Chroma

Color spaces based on the luminance and chroma has the same properties. The first component Y represents the luminance, whereas the other two components represent color information [8]. Color spaces' separation of luminance and color components is beneficial. Moreover, these color spaces are usually used for video and image segmentation methods. The only difference between them is the weighted values of R, G and B.

In Eq. 2.24, the conversion of RGB to YUV is given by [42].

$$\begin{bmatrix} Y \\ U \\ V \end{bmatrix} = \begin{bmatrix} 0.299 & 0.587 & 0.114 \\ -0.14713 & -0.28886 & 0.436 \\ 0.615 & -0.51499 & -0.10001 \end{bmatrix} \begin{bmatrix} R \\ G \\ B \end{bmatrix} \tag{2.24}$$

The conversion of RGB to YC_bC_r can be formulated as in computer systems [45].

$$\begin{bmatrix} Y \\ C_b \\ C_r \end{bmatrix} = \begin{bmatrix} 0.257 & 0.504 & 0.098 \\ -0.148 & -0.291 & 0.439 \\ 0.439 & -0.368 & -0.071 \end{bmatrix} \begin{bmatrix} R \\ G \\ B \end{bmatrix} + \begin{bmatrix} 16 \\ 128 \\ 128 \end{bmatrix} \tag{2.25}$$

where RGB color space is in the range of [0-255].

The following equation gives the transformation of RGB to YIQ [45]

$$\begin{bmatrix} Y \\ I \\ Q \end{bmatrix} = \begin{bmatrix} 0.299 & 0.587 & 0.114 \\ 0.596 & -0.274 & -0.322 \\ 0.211 & -0.523 & 0.312 \end{bmatrix} \begin{bmatrix} R \\ G \\ B \end{bmatrix} \tag{2.26}$$

2.2.6 $C_1C_2C_3$

$C_1C_2C_3$ color space is a nonlinear transformation of RGB. The transformation expression is given in the following.

$$C_1 = \arctan \frac{R}{max(G, B)} \tag{2.27}$$

$$C_2 = \arctan \frac{G}{max(R, B)} \tag{2.28}$$

$$C_3 = \arctan \frac{B}{max(G, R)} \tag{2.29}$$

Gevers et. al [20] suggest this color space to help object recognition by using the effect of each band. Since shadow pixels have high blue band value and since the bigger value between green and red bands has close to blue band value, high values of C_3 component may be belongs to shadow pixels. Therefore, the color space is mostly used to detect shadows [41], [4], [21].

CHAPTER 3

LITERATURE

3.1 Literature of Shadow Detection Methods

In this chapter, we provide an overview about the shadow detection methods. Various methods to detect shadows in remote sensing images are presented in the literature. These methods can be classified with different taxonomies. Fredembach suggests a classification which distinguishes shadow detection methods into two parts: Image-based methods and user interaction methods [18]. In the first category, the shadow properties such as color, shadow structure and boundaries are taken advantages, while in the second one user interaction or some priori knowledge such as 3D geometry of the scene or sun orientation is required for detection. On the other hand, Adelina et. al do not find it sufficient to classify the approaches [1]. They in addition to these two categories, included physics based and machine learning methods in the taxonomy of shadow detection methods. Physics based methods use illumination, atmospheric conditions or material reflectance. Moreover, knowledge about the reference signature is required in machine learning methods. However, image-based methods and user interaction methods proposed in the first taxonomy contains the additional methods mentioned in second proposed taxonomy. Therefore, to distinguish the methods to two parts can be sufficient, but some index based methods require user interaction on choosing the optimal threshold point. As a result, we can classify the algorithms as model based and index based methods which are commonly used in taxonomies [4], [25]

3.1.1 Model Based Methods

In model based methods, some methods need geometric information of the scene, whereas others utilize physical information of the image to detect shadows.

The methods based on geometric information require Digital Surface Model (DSM) image and the knowledge of sun orientation. Therefore, the success of these methods depends on the quality of DSM image. DSM image may be obtained both manually [39] and through Airborne Laser Scanner (ALS) technique [33], [32], [48] to acquire 3D information of the image. In Fig. 3.1 a multispectral image and its DSM image are shown.

In physics based methods for conversion of the radiance to reflectance value, the

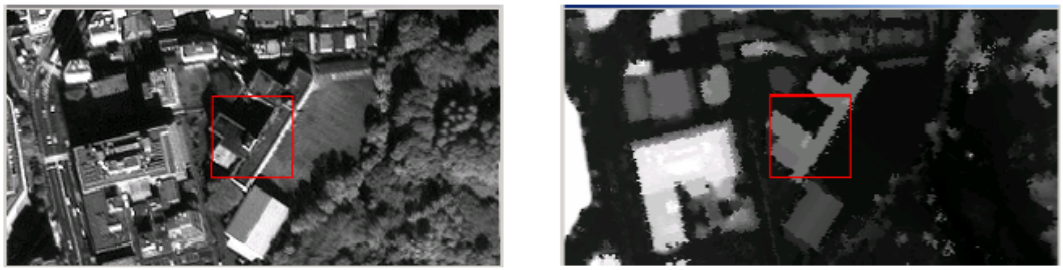

Figure 3.1: A multispectral image and its DSM image [33]

methods need the sun and viewing angles and the knowledge of aerosol abundance [1]. Since acquiring such information is difficult, these methods are not preferred. The methods are usually applied on hyperspectral data set [2], [23].

3.1.2 Image-based Methods

Automatic shadow detection methods have become a popular research topic in remote sensing images for last decade although it is started at the end of the 70's. In high resolution imagery, shadow analysis firstly is introduced with RGB image, and then with increasing the popularity of multispectral image which has NIR band, the analyses concentrate on NIR band's effect on shadow.

Polidorio et. al contacted between shadowed area and Rayleigh Scattering [37]. Because of the Rayleigh Scattering, shadowed region is highly saturated by blue-violet when compared with other wavelengths of visible spectrum. Also, shadowed regions have lower luminance. Therefore, after RGB image is converted to HSI model, the difference of the intensity and saturation is utilized. Since intensity has lower value in shadow and saturation has higher value, the lower values of the difference belong to shadow regions. Finally, they chose different threshold points for airborne and orbital sensors.

Huang transforms RGB to HSI according to Polidorio's suggestion [25]. However, in this conversion hue is a cue to detect shadow. Shadows have higher hue value, while they have low values in blue channel. Moreover, they have small difference between green and blue. Therefore, it is suggested that these properties are applied and threshold points are determined step by step. In conclusion, the pixels which have high hue values, small blue values and small difference between green and blue are determined as shadow pixels.

Another example to the transformation the color space is to convert RGB to $C_1C_2C_3$ space. Sarabandi looks at the shadows value after C_1, C_2 and C_3 transformations are applied and points out that shadows have higher value on C_3 [41].

Dare analyzes the shadows in high resolution satellite imagery of the urban areas [13]. He uses the single band high resolution panchromatic satellite images. The intensity values over 255 is fixed as 255 and the remaining pixels retain their original values since the shadow region is only in this range. Then he utilized from the histogram thresholding to detect shadow pixels. The mean of two peaks is chosen as

the thresholding value. After that, regions are encoded such that all unconnected regions are encoded uniquely. And finally, since water regions are included among the shadow regions, the water regions which have small variance of the encoded regions are extracted from the shadowed region. However, the variance threshold is decided by examination of the image. The algorithm is tested on IKONOS and Quickbird images.

Tsai uses the information given by Polidorio which the intensity has low value in shadow region [45]. Moreover, he appends the information that hue value increases in shadow region. In the light of these information, RGB images are transferred to the different color spaces such as HSI, HSV, HCV, YIQ, and YC_bC_r. Then some ratios are suggested and Otsu's method is applied for detecting shadowed and non-shadow area by an automatic thresholding [36]. These methods are tested on aerial images and it is claimed that the results obtained by HSI, YIQ and YC_bC_r are more successful.

Chen researches the behavior of each band [10]. For each band and each index, he proposes a method to determine the threshold value. If the histogram has two discrete peaks, the valley is taken as decision surface and if the histogram has two close peaks, there would be a new peak which is taken as decision surface. As a result, he suggests some indexes and applies them on Quickbird images. After the results, he proposes an index based on RGB to distinguish the water and shadow.

Arevalo et. al use C_3 component to detect shadow pixels [4]. However, they suggest that the component is not sufficient to detect shadows and so a region growing method based on intensity and saturation value is suggested. If the neighborhood pixels of shadow pixels have higher saturation and lower intensity values than determined threshold points, the region growing is applied. This allows remaining gaps in shadow regions to be added to the shadow pixels.

A new ratio map based on Tsai's ratio is proposed by Chung [11]. He utilizes the Tsai's ratio, and by using it, an exponential function is established to increase the gap between the Tsai's ratio values of shadow and non-shadow pixels. Moreover, the process consists of two parts: detection of candidate shadow pixels and detection of true shadow pixels. In the first part, the candidate shadow pixels are detected by using the ratio mentioned above and using the Otsu's method. Then, for grouping the shadow region, connected component analysis is applied to the candidate shadow region in the second part. Finally, a global ratio map and thresholding is performed to each candidate shadow region. In addition, Chung compares the proposed method, Tsai's method and Huang's method, and asserts that the best algorithm is the proposed method.

Fredembach and Süsstrunk introduce a map which is based on visible bands to NIR ratio [18]. Firstly, it is dwelled on that in shadow region, pixels have less value than non-shadow region. Therefore, with the help of a formula, candidate shadows which have less value are distinguished from non-shadow regions. Then, it is utilized from the information that skylight emits in NIR band less than visible bands, however, sunlight emits in NIR band as much as visible bands. In the light of this information, a ratio is used which is visible bands to NIR. If the maximum ratio is smaller 2, it will be a sunlit region, otherwise it may be shadow. By taking into consideration these two states, a shadow map is constructed. Finally, after the first valley of the

histogram is selected as a threshold on the shadow map, the binary map is created to shadow detection.

Cai et. al apply different maps based on HSI color space [7]. The first map is the difference suggested by Polidorio et. al [37]. Second map is the ratio of saturation and intensity and the last map is normalized difference of the first map. After Otsu thresholding is applied to these maps, the combination of the pixels, which belong to lower values of the difference and normalized difference and higher values of the ratio than threshold points respectively, are selected as shadow pixel candidates. Since these pixels include vegetation pixels as well, Normalized Difference Vegetation Index (NDVI) is applied to separate vegetation and shadow pixels.

Teke presents a new approach to shadow detection by using the false color image [43]. Since blue band scatters most in shadow region, the pixels have higher value in blue band than red and NIR band. On the other hand, red, green and NIR has low values in shadow region. To obtain a dark region to detect shadow, RGB color space is converted to NIR-R-G color space. Then, based on Polidorio's suggestion, a ratio map is proposed. Because vegetation region and dark objects have similar the difference of saturation and intensity and vegetation region has higher values than shadow, the proposed ratio is difference over sum of them. Then, to distinguish the shadow parts, Otsu thresholding is applied. Finally, the candidate shadow pixels include vegetation parts, so NDVI is used to separate true shadow pixels. Teke claims that this method works better results except for images which include water region.

CHAPTER 4

COMPARISON OF SHADOW DETECTION METHODS

4.1 Methods

In this section, the methods based on ratio which are mentioned in Section 3 are explained and novel ratios are proposed. The methods are applied for both visible and NIR bands in order to show their effects. As mentioned in Section 2.1.2, shadows have darker values. However, blue band value is higher than NIR and red bands values in a shadow region and so it increases the shadow intensity. Therefore, when NIR band is used instead of blue band, shadows become darker than non-shadow regions. As a result, false color images that are a combination of NIR-Red-Green bands, give better results on shadow detection [43], [3]. In Fig. 4.1, true and false color images are shown. The dark region belongs to shadow on these images.

(a) True image (b) False color

Figure 4.1: True and false color images

4.1.1 Methods Based on Saturation and Intensity

Based on the shadow properties mentioned on section 2.1.2, shadow region has high saturation (S), whereas it has low intensity (I) values. Therefore, Polidorio et. al [37]

Figure 4.2: Result of Polidorio et. al suggestion

suggest a difference expressed as $I - S$ and so shadow and non-shadow regions have low and high values, respectively on the difference image. The result image is shown in Fig. 4.2. However, low values on the result image belong to not only shadow pixels, but also vegetation, dark objects and water pixels. On the other hand, vegetation pixels have higher saturation and intensity values than shadow pixels. Therefore, Teke et. al [43] propose a ratio map given in 4.1 which Polidorio's difference is divided by the sum of saturation and intensity values. Thus, similarity of the values on vegetation and shadow pixels decreases.

$$Ratiomap = \frac{S - I}{S + I} \tag{4.1}$$

The result of the image applied ratio map to true color image in Fig. 4.3 and the result of the image applied ratio map to false color image, given in Fig.4.4 are more separable when compared to Polidorio's difference. In Figure 4.4, shadow regions have high values. Besides, in false color image some vegetation areas have lower values when compared to true color image. Therefore, to separate the shadow pixels from the vegetation pixels, false color image is more useful.

4.1.2 Methods Based on Hue and Intensity

Shadow pixels have higher hue values than their surroundings. Huang [25] bases it to the property of shadow given in Expression (2.13) that the change between shadow and non-shadow region in red band value is highest, while the change in blue band is

Figure 4.3: Result of Teke's ratio map on true color

Figure 4.4: Result of Teke's ratio map on false color

Figure 4.5: Hue of the true color image

lowest value in RGB image. He gives RGB to hue (H) conversion such as

$$H = \arctan\left(\frac{\sqrt{3}(G-B)}{(R-G)+(R-B)}\right) \tag{4.2}$$

The pixels color value changes to $(R-\Delta R, G-\Delta G, B-\Delta B)$ after they are shadowed. Afterwards, hue value changes to

$$H' = \arctan\left(\frac{\sqrt{3}((G-B)-(\Delta G-\Delta B))}{(R-G)+(R-B)-(2\Delta R-\Delta G-\Delta B)}\right) \tag{4.3}$$

Since shadows usually form on asphalt or greenish grasslands in aerial images, their green value is higher than their blue value [25]. When this information and (2.13) are taken into consideration, hue values on the shadow pixels (4.3) are clearly higher than non-shadow region. On the other hand, on asphalt and greenish grasslands, NIR band has higher value than other bands. After maximum change is formed on NIR band value in shadow region, hue value decreases on shadow region in false color images. Hue images of true and false color image can be seen in Fig. 4.5 and in Fig. 4.6 respectively.

Tsai [45] utilizes both high hue and low intensity values of HSI color space in true color images, so he suggests the following ratio map.

$$RatioMap_{HSI} = \frac{H+1}{I+1} \tag{4.4}$$

The ratio map provides to obtain higher values on shadow regions in true color images, and the result image is shown in Fig. 4.7. Although hue values on shadow

Figure 4.6: Hue of the false color image

regions are lower than non-shadow regions except roof and water pixels in false color images, the intensity values on shadow region are smaller than non-shadow region. Therefore, highest values belong to shadow pixels on the ratio map in false color image. Fig. 4.8 is the result image of the ratio map in false color image. Tsai [45] claims that I and H components of HSI color space are equivalent or identical to V and H components of HCV color space, respectively. So the same ratio map is suggested for HCV color space in (4.5).

$$RatioMap_{HCV} = \frac{H+1}{V+1} \tag{4.5}$$

4.1.3 Methods Based on $C_1C_2C_3$ Color Space

The $C_1C_2C_3$ color space is introduced by Gevers et. al [20] to object recognition and the space is used for shadow detection by Sarabandi et. al [41]. Since in the shadow pixels, blue component usually has higher values than other components, high values of C_3 give a cue to detect shadows. Each component of the color space is shown in Fig. 4.9. In Fig. 4.9-c, the highest values belong to shadow and vegetation pixels.

In C_3 component, since vegetation pixels also have high blue band value, some vegetation pixels have similar values to shadow pixels. To eliminate these pixels, I propose to modify the color space such as

$$C_1' = \arctan(\frac{R}{max(G, B, NIR)}) \tag{4.6}$$

Figure 4.7: Tsai's ratio map of the true color image on HSI color space

Figure 4.8: Tsai's ratio map of the false color image on HSI color space

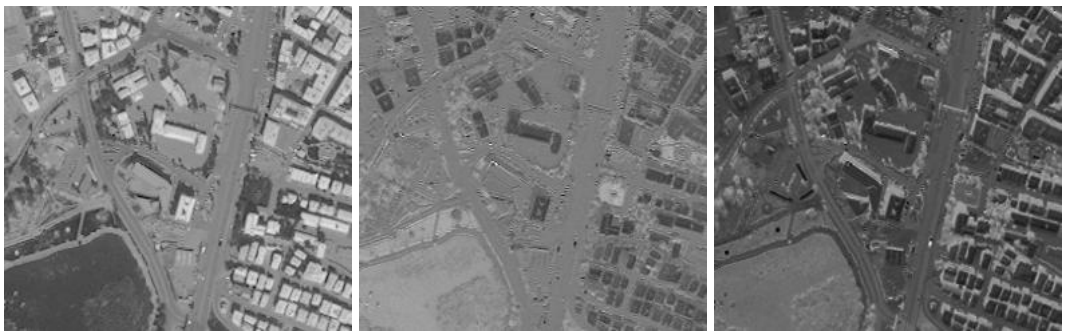

(a) C_1 (b) C_2 (c) C_3

Figure 4.9: C_1, C_2 and C_3 components of $C_1C_2C_3$ Color space

$$C_2' = \arctan(\frac{G}{max(R, B, NIR)}) \tag{4.7}$$

$$C_3' = \arctan(\frac{B}{max(G, R, NIR)}) \tag{4.8}$$

$$C_4' = \arctan(\frac{NIR}{max(R, G, B)}) \tag{4.9}$$

(a) C_1' (b) C_2'

Figure 4.10: C_1' and C_2' components of $C_1'C_2'C_3'C_4'$ Color space

C_3' helps to separate shadow and vegetation pixels because in vegetation pixels, NIR band has the maximum value. Thus, C_3' component has lower values than C_3 component for vegetation pixels. On the other hand, NIR band value seen in Fig. 4.12 is low for water pixels. Thus, the normalized C_3' component also gives higher values on water pixels than the normalized C_3. Therefore, it is proposed that in the first step, the image is transformed from RGB to $C_1C_2C_3$ and the result image is normalized.Then, a threshold value T_1 is determined for separating high values of C_3 to obtain candidate shadow pixels

$$S(i, j) = \{(i, j) \quad | \quad C_3(i, j) > T_1\} \tag{4.10}$$

(a) C'_3 (b) C'_4

Figure 4.11: C'_3 and C'_4 components of $C'_1C'_2C'_3C'_4$ Color space

Figure 4.12: NIR band of the image

In the second step, the image is transformed from RGB to $C_1'C_2'C_3'C_4'$ and again, the result image is normalized. Similarly, another threshold value T_2 is determined for eliminating vegetation pixels. Finally, the intersection of the pixels is chosen as the shadow map

$$S'(i,j) = S(i,j) \cap \{(i,j) \quad | \quad C_3'(i,j) > T_2\} \tag{4.11}$$

4.1.4 Methods Based on Luminance and Chroma

Y component of the color spaces YUV, YIQ, YC_bC_r has high value on both true color image and false color image shadow pixels. They are shown on Fig. 4.13 and Fig.4.14.

(a) (b) (c)

Figure 4.13: Y components of (a)YUV, (b)YIQ, (c)YC_bC_r color spaces on true color image

(a) (b) (c)

Figure 4.14: Y components of (a)YUV, (b)YIQ, (c)YC_bC_r color spaces on false color image

However, the effect of the other components related with chroma changes on shadow pixels. In YUV color space, U component has higher values on true and false color image shadow pixels, while Y component has lower values. Therefore, $U - Y$ difference gives shadow pixels, but it gives not only shadow pixels, but also water, black objects and asphalt pixels. Yet, black objects and asphalt pixels have higher values

than shadow pixels. Thus, I propose the following ratio:

$$Ratio_{YUV} = \frac{U - Y}{U + Y} \tag{4.12}$$

Since YC_bC_r color space has the same properties in common with YUV color space, the ratio (4.13) is proposed to detect shadow pixels.

$$Ratio_{YC_bC_r} = \frac{C_b - Y}{C_b + Y} \tag{4.13}$$

Contrary to YUV and YC_bC_r, in YIQ color space, I component which is the first component of the chroma has low value on both true and false color image shadow pixels. On the other hand, Q component has high values on true color image shadow pixels, whereas it has low values on false color image shadow pixels. Therefore, the ratio in (4.14) is proposed for only true color image.

$$Ratio_{YIQ} = \frac{Q - Y}{Q + Y} \tag{4.14}$$

On the false color image, since the maximum change between shadow and non-shadow pixels which is showed on 4.15 is on the Y component of YIQ color space, Y component is proposed as distinctive property on false color image.

(a) Y (b) I (c) Q

Figure 4.15: Y, I and Q components of YIQ color spaces on false color image respectively

4.2 Selecting Automatic Threshold Point

The success of the algorithms changes according to the selection of threshold points. Therefore, an automatic threshold point must be used to detect a shadow map. The commonly used method is Otsu's threholding [36]. In this method, the idea that there is always shadow in the scene is assumed. The threshold point T which maximizes the following expression is determined by

$$Ratio(T) = \frac{(\bar{\mu}.\omega(T) - \mu(T))^2}{\omega(T).\mu(T)} \tag{4.15}$$

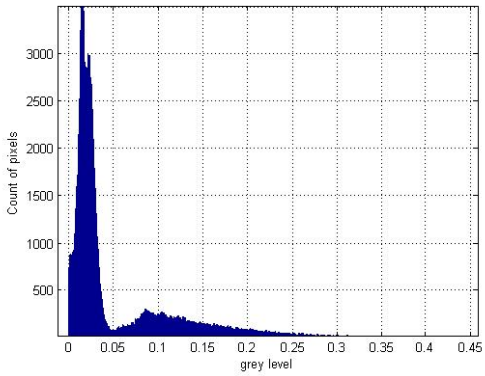

Figure 4.16: Histogram of image implemented a ratio with two classes

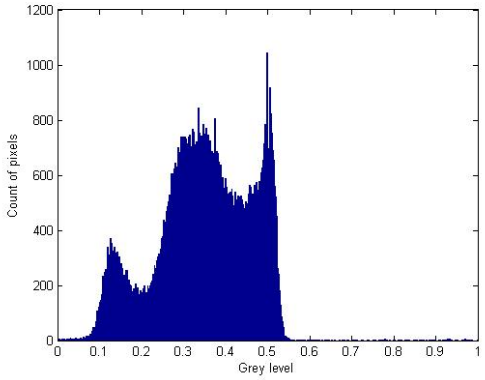

Figure 4.17: Histogram of image implemented a ratio with three classes

where $\omega(T) = \sum_{i=0}^{T} P_i$, $\mu(T) = \sum_{i=T+1}^{N} P_i$, $\bar{\mu} = \sum_{i=0}^{N} i.P_i$ and while P_i is the probability of pixels in the image, N is the maximum possible quantization level and $N = 255$ for 8 bit image components. Moreover, *Ratio* denotes the ratios which are given in above Section 4.1. Threshold point helps separate pixels into two classes while maximizing the variance between these two classes. For example, in the histogram given in Fig. 4.16, threshold point of $T = 0.0505$ is selected automatically. However, some ratios separate the pixels into more than two classes. In such situations, Otsu thresholding is applied twice. In the first step, automatic threshold point is selected by Otsu thresholding for detecting candidate shadow pixels. Then, a new automatic threshold point is selected by Otsu's method among candidate shadow pixels. For example, Fig. 4.17 shows the histogram with three classes. The first threshold point of $T = 0.3373$ is selected, then the second threshold point of $T = 0.4314$ is selected for separating shadow pixels.

CHAPTER 5

EXPERIMENTS

In this section, experimental results and the way of measurement success will be mentioned. Firstly, the dataset which is used in the thesis is introduced. Then, metrics is defined to verify the algorithms with ground truths. Finally, the results is given both numerically and visually. The proposed methods are compared with the methods in the literature.

5.1 Dataset

In this thesis, the aim is to detect shadows authomatically by using new ratios. The ratios are applied on Worldview-2 images. Worldview-2 images are obtained by WorldView-2 satellite sensor. The satellite has been launced on October 8, 2009 by Digital Globe and Worldview-2 is the third satellite of Digital Globe following the Quickbird and WorldView-1.

The sensor provides 8 bands multispectral and panchromatic imagery with 1.84 m and 0.46 m resolution, respectively. The widely known multispectral images such as IKONOS, GeoEye-1 and Quickbird satellites, have Blue, Green, Red and NIR1 multispectral bands. The different bands of Worldview-2 are coastal blue, yellow, red edge and NIR2. The spectral properties of these bands are shown in Table 5.1 and the comparison of the satellites are represented in Fig. 5.1.

Table 5.1: Spectral properties of the Worldview-2 bands

Bands	**Wavelength (μm)**
Coastal Blue	400-450
Blue	450-510
Green	510-580
Yellow	585-625
Red	630-690
Red Edge	705-745
NIR1	770-895
NIR2	860-1040

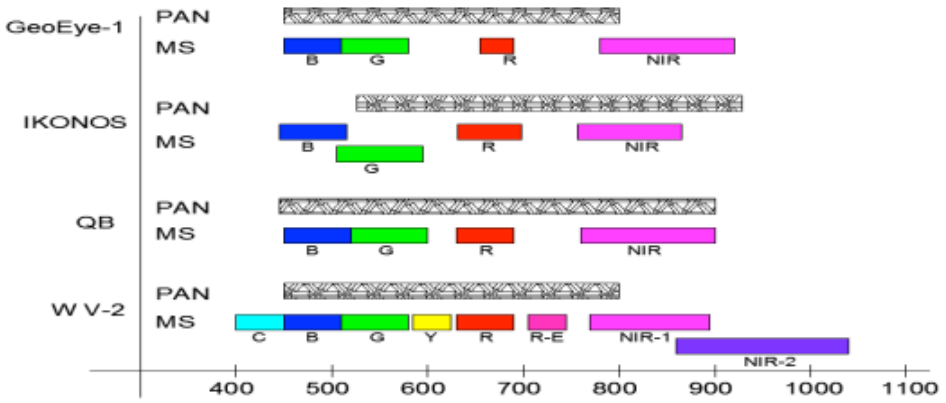

Figure 5.1: Multispectral wavelength for different satellites [16]

In this thesis, we used two multispectral Worldwiew II images covering Ankara on 30 August 2011 and 26 September 2011. Three images were cropped from the image acquired on August 30 for using with groundtruth maps. First image includes a swimming pool for blue water. Second image includes 'Mogan Lake' and the last image includes an area with high density buildings. Four more images are cropped from the image acquired on September 26 covering Yenimahalle region of Ankara. Two of them include water canal. Since the images do not have groundtruth maps, their results are presented for visual inspection on APPENDIX A.

(a) (b)

Figure 5.2: (a) RGB of the first image (b) Groundtruth of the first image

(a)

(b)

Figure 5.3: (a) RGB of the second image (b) Groundtruth of the second image

(a)

(b)

Figure 5.4: (a) RGB of the third image (b) Groundtruth of the third image

The white points represent the shadow pixels in the groundtruths of the images and the black points are not known with certainty whether they are shadow or non-shadow pixels.

One of the aim of the thesis is to compare the results of RGB, 4-Band and 8-Band images. Since we do not have the images for the same locations, appropriate bands of Worldview-2 are used for RGB and 4-Band images. RGB images consist of Red, Green and Blue bands, while in 4-Band images NIR1 band is added to RGB bands according to Fig. 5.1. As a result, RGB images represent the true color images whereas for NIR band of false color images, NIR1 is used in 4-Band images and NIR2 is used in 8-Band images.

5.2 Verification

There are some metrics to evaluate the algorithms. These metrics are computed as comparing the ground truth and proposed shadow maps. Our shadow maps are constructed according to the threshold points after the ratio is applied to the image and the threshold point is selected. Then, precision, recall and F-measure metrics are used to compare these shadow maps. The variables of the metrics are defined below.

- **True Positive (TP)** : The number of pixels that determined as shadow in both ground truth and proposed shadow map.
- **False Positive (FP)** : The number of pixels that determined as shadow in proposed shadow map and non-shadow in ground truth.
- **True Negative (TN)** : The number of pixels that determined as non-shadow in both ground truth and proposed shadow map.
- **False Negative (FN)** : The number of shadow pixels that are determined as non-shadow in proposed shadow map.

5.2.1 Precision

Precision is a measurement of a percentage of the pixels that are detected correctly as shadow. Expression (5.1) gives the calculation of the precision.

$$Precision = \frac{TP}{TP + FP} \tag{5.1}$$

In other words, it can be summarized as follows:

$$Precision = \frac{the\ number\ of\ pixels\ determined\ as\ shadows\ correctly}{the\ number\ of\ pixels\ determined\ as\ shadows} \tag{5.2}$$

5.2.2 Recall

Recall is a measurement of a percentage that gives how many shadow pixels are detected. The equation (5.3) shows the calculation of recall.

$$Precision = \frac{TP}{TP + FN} \tag{5.3}$$

Also, it can be written as:

$$Precision = \frac{the\ number\ of\ pixels\ determined\ as\ shadows\ correctly}{the\ number\ of\ pixels\ given\ as\ shadow\ in\ groundtruth} \tag{5.4}$$

5.2.3 F-measure

Recall and precision are inversely related functions. Often while precision value increases, recall value decreases. Decreasing precision value means that false pixels are detected. On the other hand, decreasing recall value means that true pixels are not detected. For obtaining a single metric, F-measure is used. F-measure is harmonic mean of these two metrics, so the maximum value of f-measure is accepted as optimum value for the measurement.

$$F_1 = 2 * \frac{Precision * Recall}{Precision + Recall} \tag{5.5}$$

5.3 Experimental Results

In this section, firstly the results of the success of selected threshold point are given. Then the results of the ratios is represented by numerically and visually.

5.3.1 Results of Selected Threshold Point

In the (a) part of the figures (5.5) - (5.18) histograms of the images are given. On histograms, the maximum value of fmeasure and the threshold points, which are selected if Otsu thresholding is applied one or two times, are specified. The time for applying Otsu thresholding is determined according to these histograms. After it is determined, in the (b) parts of the figures (5.5) - (5.18), how Otsu thresholding is near to optimal threshold point is shown. The top point of the fmeasure corresponding to threshold point is the optimal threshold points.

As a result of this information, the ratio (4.1) based on saturation and intensity on false color image and the ratio (4.5) based on HCV color space separate the pixels into two parts, so Otsu thresholding is applied once. On the other hand, since the

other algorithms which are based on the ratio (4.1) based on saturation and intensity on true color image, HSI, $C_1C_2C_3$, YUV, YC_bC_r and YIQ color spaces separates the pixels into more than two classes, Otsu thresholding is applied twice as described in Section 4.2.

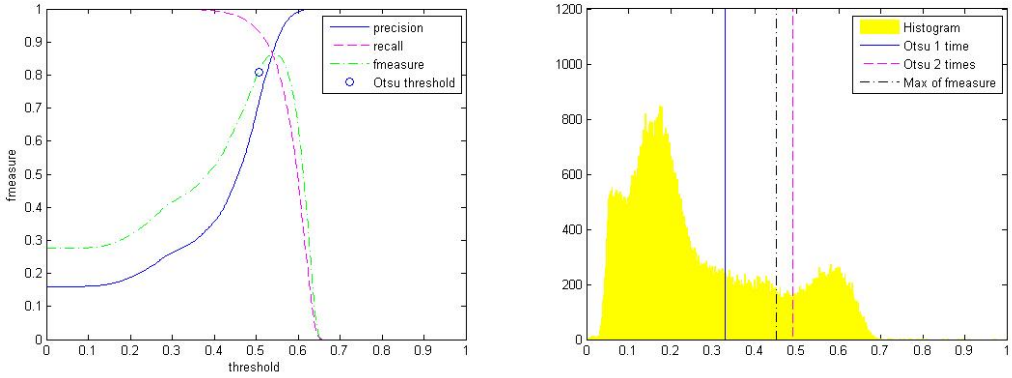

Figure 5.5: a) Automatic threshold point on ratio based on Saturation and Intensity on true color image b) Histogram of ratio based on Saturation and Intensity on true color image

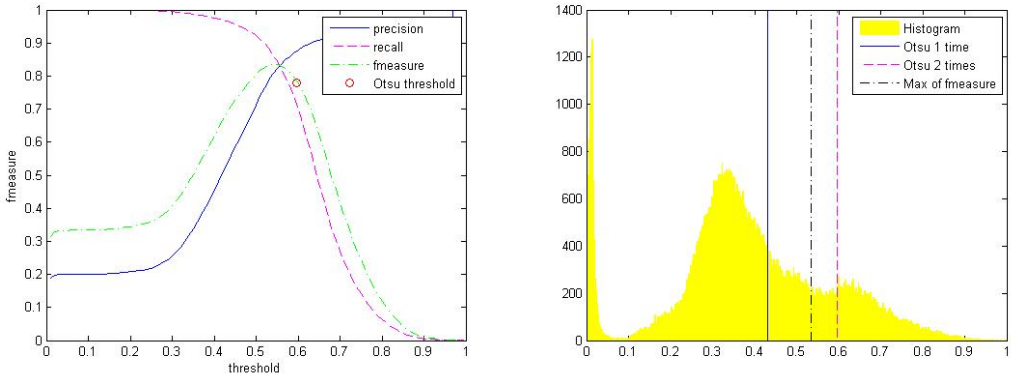

Figure 5.6: a) Automatic threshold point on ratio based on Saturation and Intensity on false color image b) Histogram of ratio based on Saturation and Intensity on false color image

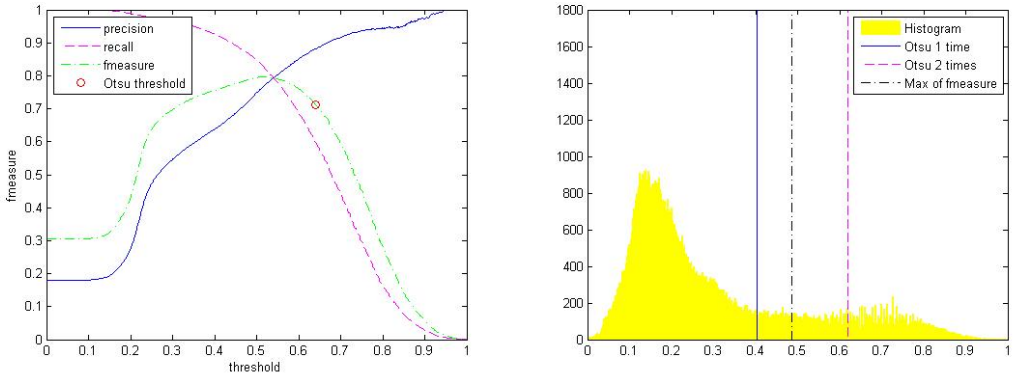

Figure 5.7: a) Automatic threshold point on ratio based on Hue and Intensity on false color image b) Histogram of ratio based on Saturation and Intensity on false color image

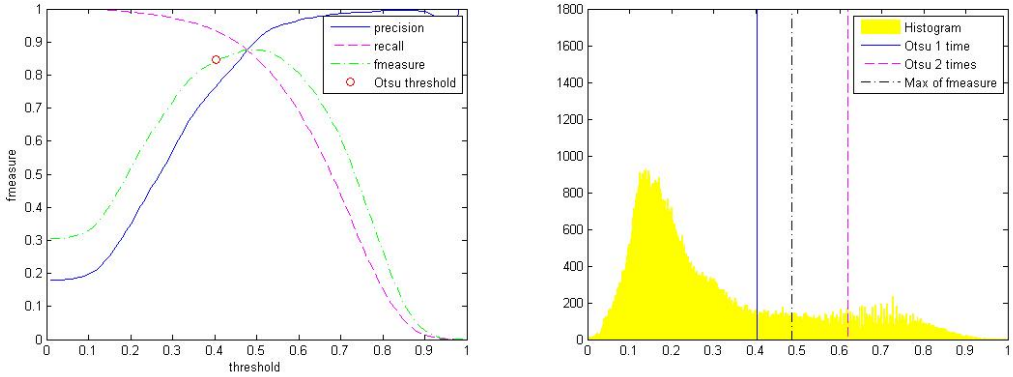

Figure 5.8: a) Automatic threshold point on ratio based on Hue and Intensity on false color image b) Histogram of ratio based on Hue and Intensity on false color image

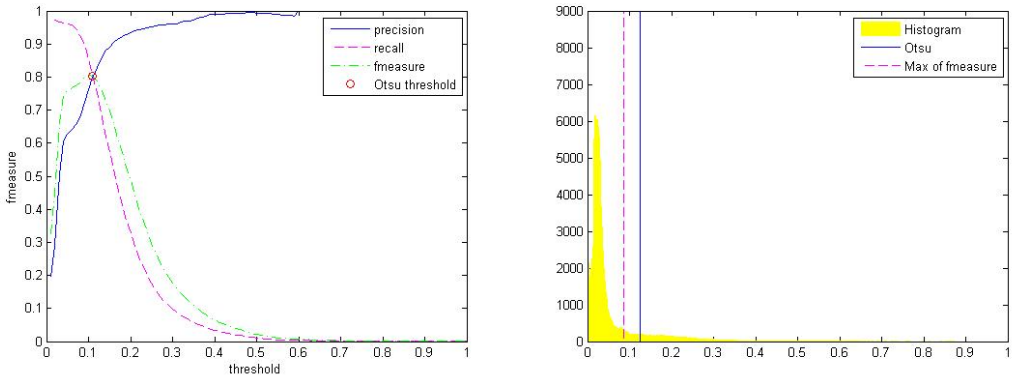

Figure 5.9: a) Automatic threshold point on HCV color space with true color image b) Histogram of HCV color space with true color image

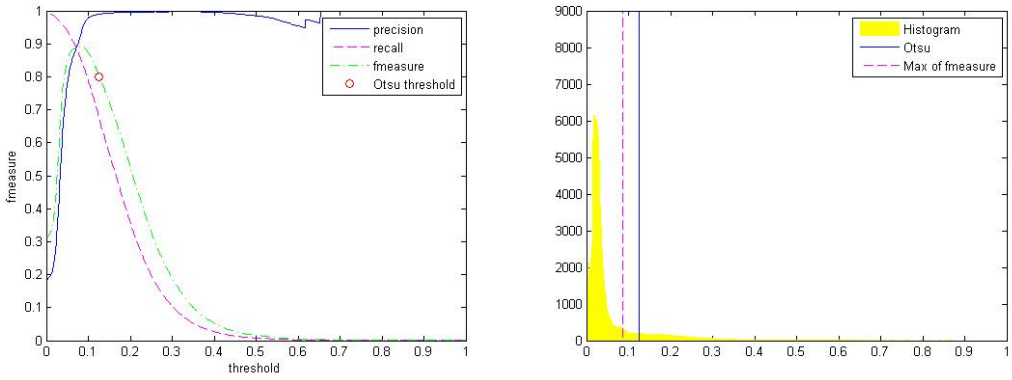

Figure 5.10: a) Automatic threshold point on HCV color space with false color image b) Histogram of HCV color space with false color image

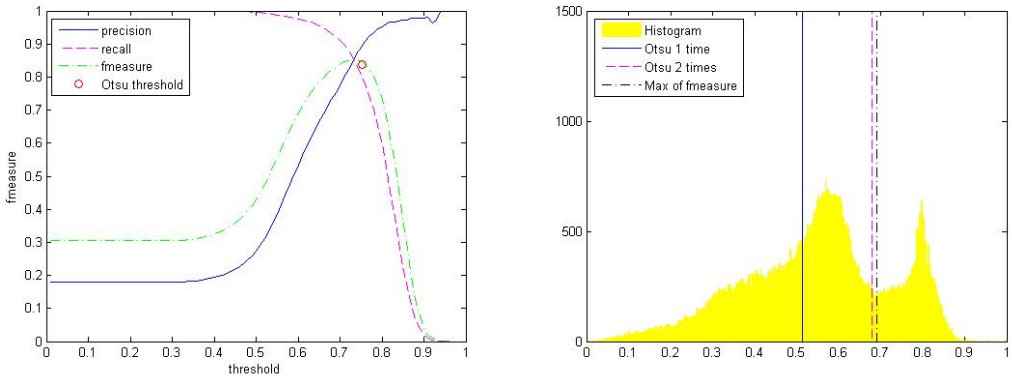

Figure 5.11: a) Automatic threshold point on $C_1C_2C_3$ color space with true color image b) Histogram of $C_1C_2C_3$ color space with true color image

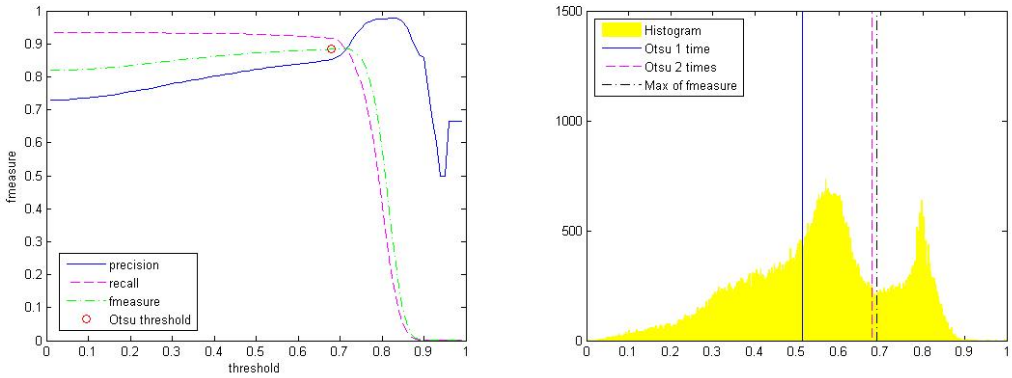

Figure 5.12: a) Automatic threshold point on $C_1C_2C_3$ color space with false color image b) Histogram of $C_1C_2C_3$ color space with false color image

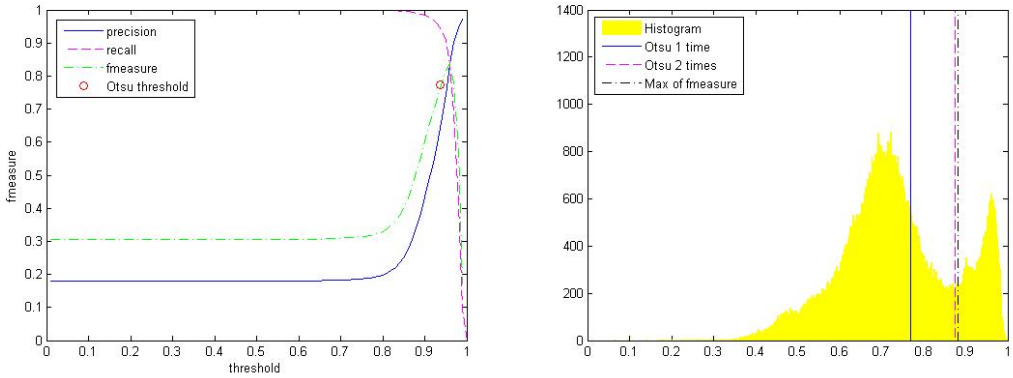

Figure 5.13: (a) Automatic threshold point on YUV color space with true color image (b) Histogram of YUV color space with true color image

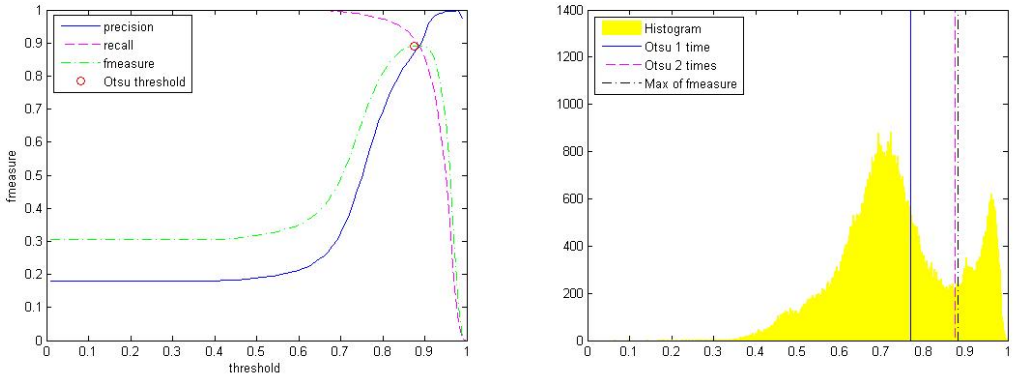

Figure 5.14: (a) Automatic threshold point on YUV color space with false color image (b) Histogram of YUV color space with false color image

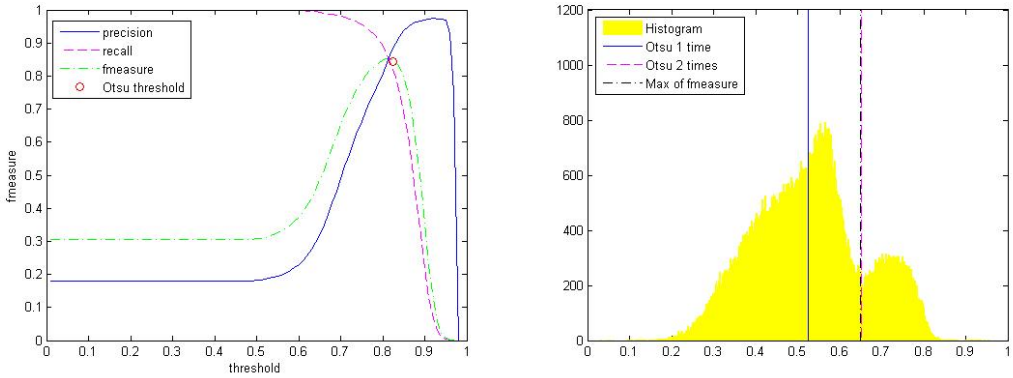

Figure 5.15: (a) Automatic threshold point on YC_bC_r color space with true color image (b) Histogram of YC_bC_r color space with true color image

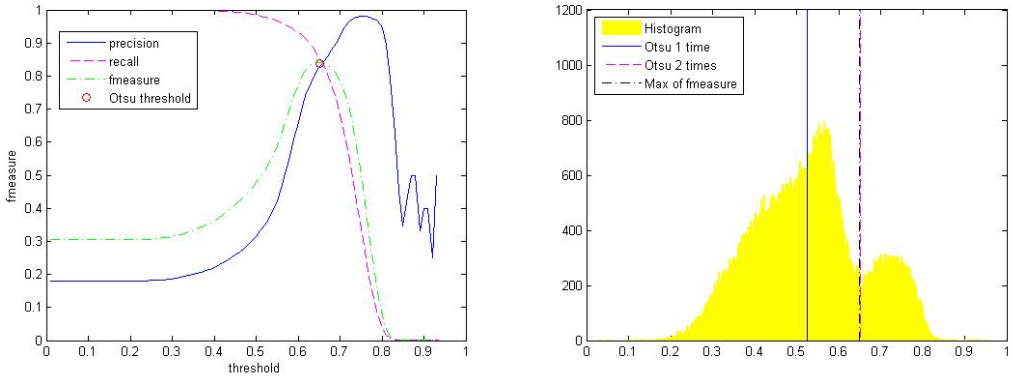

Figure 5.16: (a) Automatic threshold point on YC_bC_r color space with false color image (b) Histogram of YC_bC_r color space with false color image

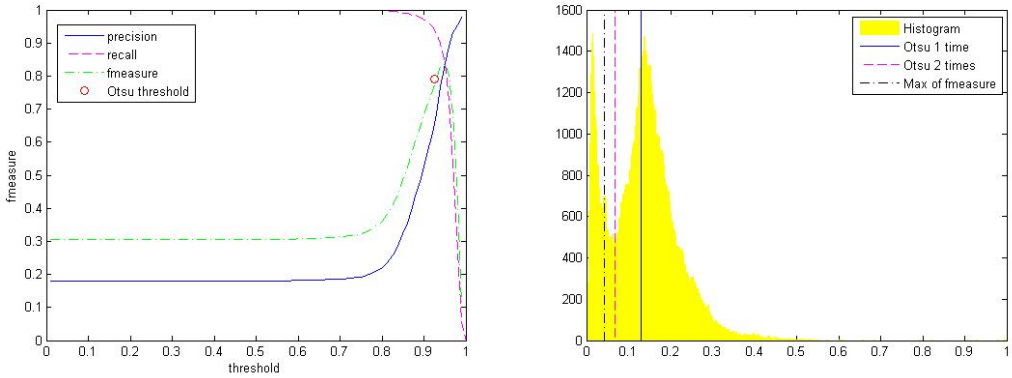

Figure 5.17: (a) Automatic threshold point on YIQ color space with true color image (b) Histogram of YIQ color space with true color image

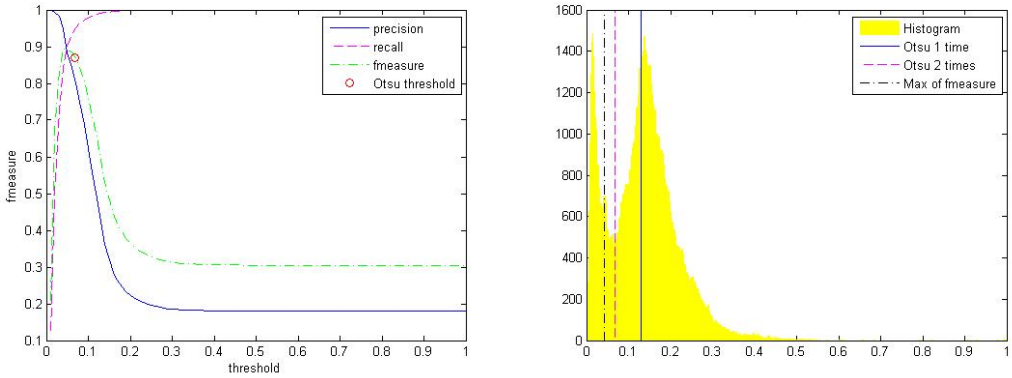

Figure 5.18: (a) Automatic threshold point on YIQ color space with false color image (b) Histogram of YIQ color space with false color image

5.3.2 Results of Applied Ratios

The proposed ratios and the ratios in the literature are compared both numerically and visually. In the figures (5.23)-(5.70) the result images of true color images are formed by using Blue, Green and Red bands. Also, the result images of false color images are formed by using Green, Red and NIR2 bands. In the figures (5.23)-(5.70), green, blue, red and white pixels represent TP, TN, FP and FN values, respectively.

The ratio based on saturation and intensity on true color images suggested by Polidorio et. al [37] and Cai et. al [7] captures grass and vegetation pixels extremely as shadow and the ratio on false color images suggested by Teke et. al [43] captures less grass and water pixels incorrectly.

When the ratio based on hue and intensity with using HSI color space is applied, few vegetation pixels are found as shadow on true color images and few vegetation and roof pixels are found as on false color images. Moreover, some shadow pixels can not be captured on both false and true color images.

The ratio based on HCV color space does not find lake water pixels as shadow on true and false color images. Besides, on true color images, some vegetation pixels are detected as shadow. On the other hand, all shadow pixels are not detected on true and false color images.

C_3 component capture some vegetation pixels as shadow. Therefore we suggest a new C_3 component to eliminate these vegetation pixels. However, new C_3 component water pixels as shadow. As a result, we propose the intersection of C_3 and C_3' components which gives better results. The weakness of it is to not detect self shadow pixels.

The result images cropped from Yenimahalle region image gave similar results to the images which have groundtruth maps. The combination of C_3 and new proposed C_3 components can detect shadows successfully on these images. Besides, successful results are also obtained by the color spaces based on luminance and chroma (YUV, YC_bC_r, YIQ) except for water pixels. The water and shadow areas could not be distinguished. Moreover, the result images on APPENDIX A show that false color images are more helpful to detect shadow pixels than true color images except for the ratios based on hue and intensity and YC_bC_r.

The ratios based on luminance and chroma can not detect self shadow pixels on the false color of the first image. Moreover, lake water pixels and recent asphalt road are captured as shadow pixels on false color images. On true color images, recent asphalt road, grass and vegetation pixels are detected as shadow by these ratios. Also, lake water pixels are detected incorrectly by YUV and YIQ ratios.

The accuracy of the images is shown in (5.19) and numerically results are given in Table (5.2), Table (5.3) and Table (5.4). Except for the ratios based on hue-intensity and YC_bC_r, false color images gives better results. Moreover, the intersection of C_3 and C_3' components has highest accuracy on average of three images. Besides, the ratios based on luminance and chroma have very high accuracy for false color images if the image does not contain water pixels.

Table 5.2: The experimental results of the algorithms for the first image

		True color image			False color image		
	Threshold	**Precision**	**Recall**	**F-measure**	**Precision**	**Recall**	**F-measure**
$\frac{I-S}{I+S}$	Otsu	0.4888	0.9911	0.6547	0.7289	0.9956	0.8416
	Manual	0.8930	0.8414	0.8665	0.9804	0.9690	0.9747
$\frac{H_{HSI}+1}{I_{HSI}+1}$	Otsu	0.9558	0.9346	0.9451	0.9556	0.5499	0.6981
	Manual	0.9547	0.9359	0.9452	0.8494	0.9371	0.8911
$\frac{H_{HCV}+1}{V_{HCV}+1}$	Otsu	0.9888	0.6181	0.7607	0.9989	0.7390	0.8499
	Manual	0.8950	0.8159	0.8536	0.9855	0.9536	0.9693
C_3	Otsu	0.9634	0.8680	0.9132	0.9882	0.8621	0.9209
	Manual	0.9300	0.9496	0.9397	0.9843	0.8663	0.9215
$\frac{U-Y}{U+Y}$	Otsu	0.5607	0.9864	0.7150	0.9965	0.9393	0.9671
	Manual	0.9533	0.8771	0.9136	0.9859	0.9660	0.9759
$\frac{C_b-Y}{C_b+Y}$	Otsu	0.5262	0.9904	0.6873	0.9841	0.9712	0.9776
	Manual	0.9489	0.8821	0.9143	0.9808	0.9746	0.9777
$\frac{Q-Y}{Q+Y}$	Otsu	0.5621	0.9862	0.7161	0.9879	0.9682	0.9779
	Manual	0.9473	0.8844	0.9148	0.9794	0.9777	0.9786

The ratios are applied by using both NIR1 and NIR2 bands. The false color image results with NIR1 and NIR2 bands are given in Table (5.5), Table (5.6) and Table (5.7). Their comparison is represented on Fig. 5.20. The results show that NIR2 band is more helpful than NIR1 band to detect shadows.

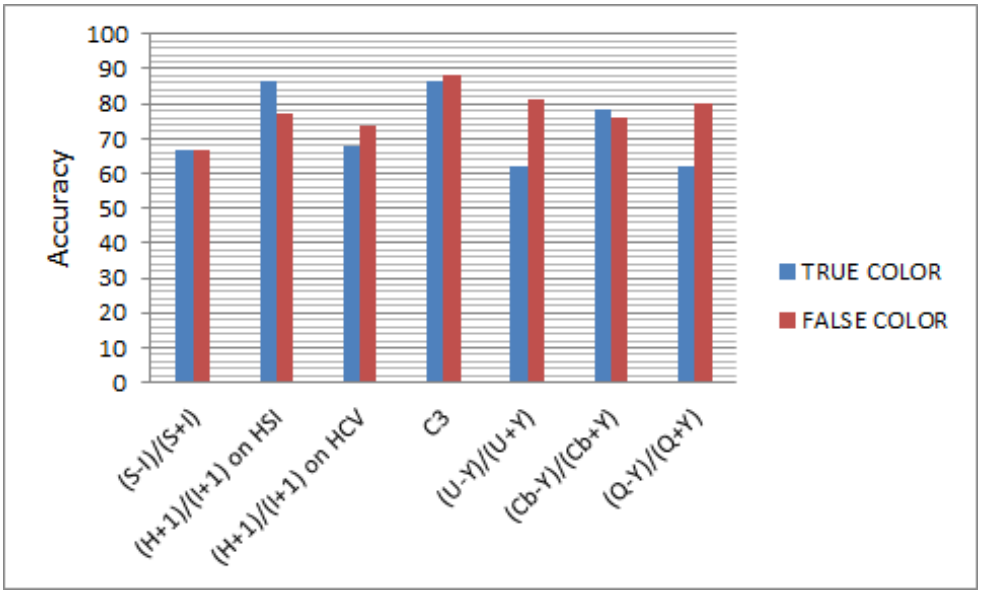

Figure 5.19: Average accuracy of the ratios for the three images

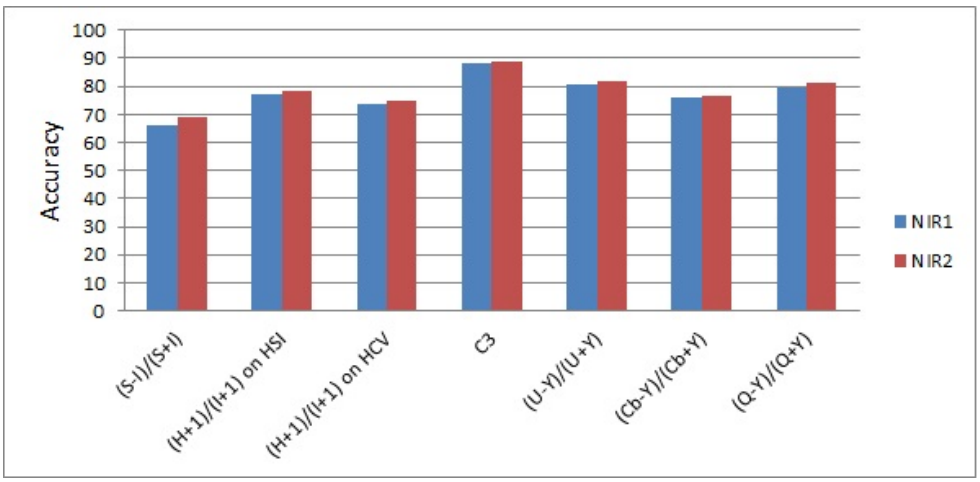

Figure 5.20: Comparison of average accuracy of the false color images by using NIR1 and NIR2

Table 5.3: The experimental results of the algorithms for the second image

		True color image			False color image		
	Threshold	**Precision**	**Recall**	**F-measure**	**Precision**	**Recall**	**F-measure**
$\frac{I-S}{I+S}$	Otsu	0.7252	0.5518	0.6267	0.3587	0.5889	0.4458
	Manual	0.7094	0.5616	0.6269	0.4011	0.8691	0.5489
$\frac{H_{HSI}+1}{I_{HSI}+1}$	Otsu	0.8473	0.7742	0.8091	0.9312	0.8062	0.8642
	Manual	0.8464	0.7752	0.8092	0.8721	0.8905	0.8812
$\frac{H_{HCV}+1}{V_{HCV}+1}$	Otsu	0.3127	0.9260	0.4675	0.4135	0.8826	0.5632
	Manual	0.6656	0.6057	0.6342	0.8333	0.4476	0.5824
C_3	Otsu	0.8551	0.8258	0.8402	0.9749	0.8111	0.8855
	Manual	0.8655	0.8185	0.8413	0.9736	0.8150	0.8874
$\frac{U-Y}{U+Y}$	Otsu	0.2384	0.9705	0.3828	0.4411	0.8974	0.5915
	Manual	0.7634	0.6904	0.7251	0.4407	0.9510	0.6023
$\frac{C_b-Y}{C_b+Y}$	Otsu	0.7740	0.8370	0.8042	0.3670	0.6475	0.4685
	Manual	0.8427	0.7838	0.8122	0.3870	0.8387	0.5296
$\frac{Q-Y}{Q+Y}$	Otsu	0.2345	0.9750	0.3781	0.4089	0.9729	0.5758
	Manual	0.7548	0.7049	0.7290	0.4347	0.9385	0.5941

Table 5.4: The experimental results of the algorithms for the third image

		True color image			False color image		
	Threshold	**Precision**	**Recall**	**F-measure**	**Precision**	**Recall**	**F-measure**
$\frac{I-S}{I+S}$	Otsu	0.8809	0.6008	0.7144	0.9213	0.6470	0.7766
	Manual	0.7619	0.8358	0.7971	0.8890	0.8661	0.8774
$\frac{H_{HSI}+1}{I_{HSI}+1}$	Otsu	0.9004	0.7811	0.8365	0.8746	0.7184	0.7889
	Manual	0.8577	0.8594	0.8585	0.7976	0.8762	0.8351
$\frac{H_{HCV}+1}{V_{HCV}+1}$	Otsu	0.7980	0.8057	0.8018	0.9844	0.7307	0.8388
	Manual	0.7545	0.8659	0.8064	0.9480	0.8417	0.8917
C_3	Otsu	0.8962	0.8001	0.8454	0.9446	0.7925	0.8619
	Manual	0.8587	0.8490	0.8538	0.9496	0.7909	0.8630
$\frac{U-Y}{U+Y}$	Otsu	0.6402	0.9458	0.7635	0.8693	0.9138	0.8910
	Manual	0.8233	0.8578	0.8402	0.8803	0.9031	0.8915
$\frac{C_b-Y}{C_b+Y}$	Otsu	0.8840	0.8209	0.8513	0.8258	0.8667	0.8458
	Manual	0.8607	0.8479	0.8542	0.8220	0.8714	0.8460
$\frac{Q-Y}{Q+Y}$	Otsu	0.6597	0.9396	0.7752	0.8142	0.9477	0.8759
	Manual	0.8225	0.8621	0.8418	0.9350	0.8590	0.8954

Table 5.5: The comparison of false color images by using NIR1 and NIR2 for the first image

	False Color Image					
	By using NIR1			**By using NIR2**		
	Precision	**Recall**	**F-measure**	**Precision**	**Recall**	**F-measure**
$\frac{I-S}{I+S}$	0.6447	0.9979	0.7833	0.7289	0.9956	0.8416
$\frac{H_{HSI}+1}{I_{HSI}+1}$	0.9439	0.5302	0.6790	0.9556	0.5490	0.6981
$\frac{H_{HCV}+1}{V_{HCV}+1}$	0.9989	0.7307	0.8444	0.9989	0.7390	0.8499
$\mathbf{C_3}$	0.9824	0.8616	0.9180	0.9882	0.8621	0.9209
$\frac{U-Y}{U+Y}$	0.9916	0.9405	0.9654	0.9965	0.9393	0.9671
$\frac{C_b-Y}{C_b+Y}$	0.9735	0.9715	0.9725	0.9841	0.9712	0.9776
$\frac{Q-Y}{Q+Y}$	0.9824	0.9630	0.9726	0.9879	0.9682	0.9779

Table 5.6: The comparison of false color images by using NIR1 and NIR2 for the second image

	False Color Image					
	By using NIR1			**By using NIR2**		
	Precision	**Recall**	**F-measure**	**Precision**	**Recall**	**F-measure**
$\frac{I-S}{I+S}$	0.3560	0.5769	0.4403	0.3587	0.5889	0.4458
$\frac{H_{HSI}+1}{I_{HSI}+1}$	0.9092	0.7855	0.8428	0.9312	0.8062	0.8642
$\frac{H_{HCV}+1}{V_{HCV}+1}$	0.4121	0.8501	0.5551	0.4135	0.8826	0.5632
$\mathbf{C_3}$	0.9752	0.8032	0.8809	0.9749	0.8111	0.8855
$\frac{U-Y}{U+Y}$	0.4222	0.9019	0.5751	0.4411	0.8974	0.5915
$\frac{C_b-Y}{C_b+Y}$	0.3555	0.6469	0.4588	0.3670	0.6475	0.4685
$\frac{Q-Y}{Q+Y}$	0.3781	0.9730	0.5446	0.4089	0.9729	0.5758

Table 5.7: The comparison of false color images by using NIR1 and NIR2 for the third image

	False Color Image					
	By using NIR1			**By using NIR2**		
	Precision	**Recall**	**F-measure**	**Precision**	**Recall**	**F-measure**
$\frac{I-S}{I+S}$	0.9626	0.6289	0.7608	0.9213	0.6470	0.7766
$\frac{H_{HSI}+1}{I_{HSI}+1}$	0.8758	0.7164	0.7882	0.8746	0.7184	0.7889
$\frac{H_{HCV}+1}{V_{HCV}+1}$	0.9896	0.6763	0.8035	0.9844	0.7307	0.8388
$\mathbf{C_3}$	0.9592	0.7542	0.8444	0.9446	0.7925	0.8619
$\frac{U-Y}{U+Y}$	0.8525	0.9174	0.8837	0.8693	0.9138	0.8910
$\frac{C_b-Y}{C_b+Y}$	0.8289	0.8542	0.8413	0.8258	0.8667	0.8458
$\frac{Q-Y}{Q+Y}$	0.8137	0.9421	0.8732	0.8142	0.9477	0.8759

Another important point is that the ratios which have high accuracy can not detect self shadow pixels on the first image. The self shadow pixels are on white buildings in this image. Moreover, in Fig. 5.21 the buildings are in white color and self shadows are not detected on these buildings. However, if the shadows are on another color building, the ratios can detect the shadows. In Fig 5.22 three buildings are pink and two buildings are light brown. Self shadow of these buildings are detected and results are shown in Fig. 5.22-b and Fig. 5.22-d.

(a)

(b)

Figure 5.21: (a) Representation of white buildings (b) shadow detection of (a)

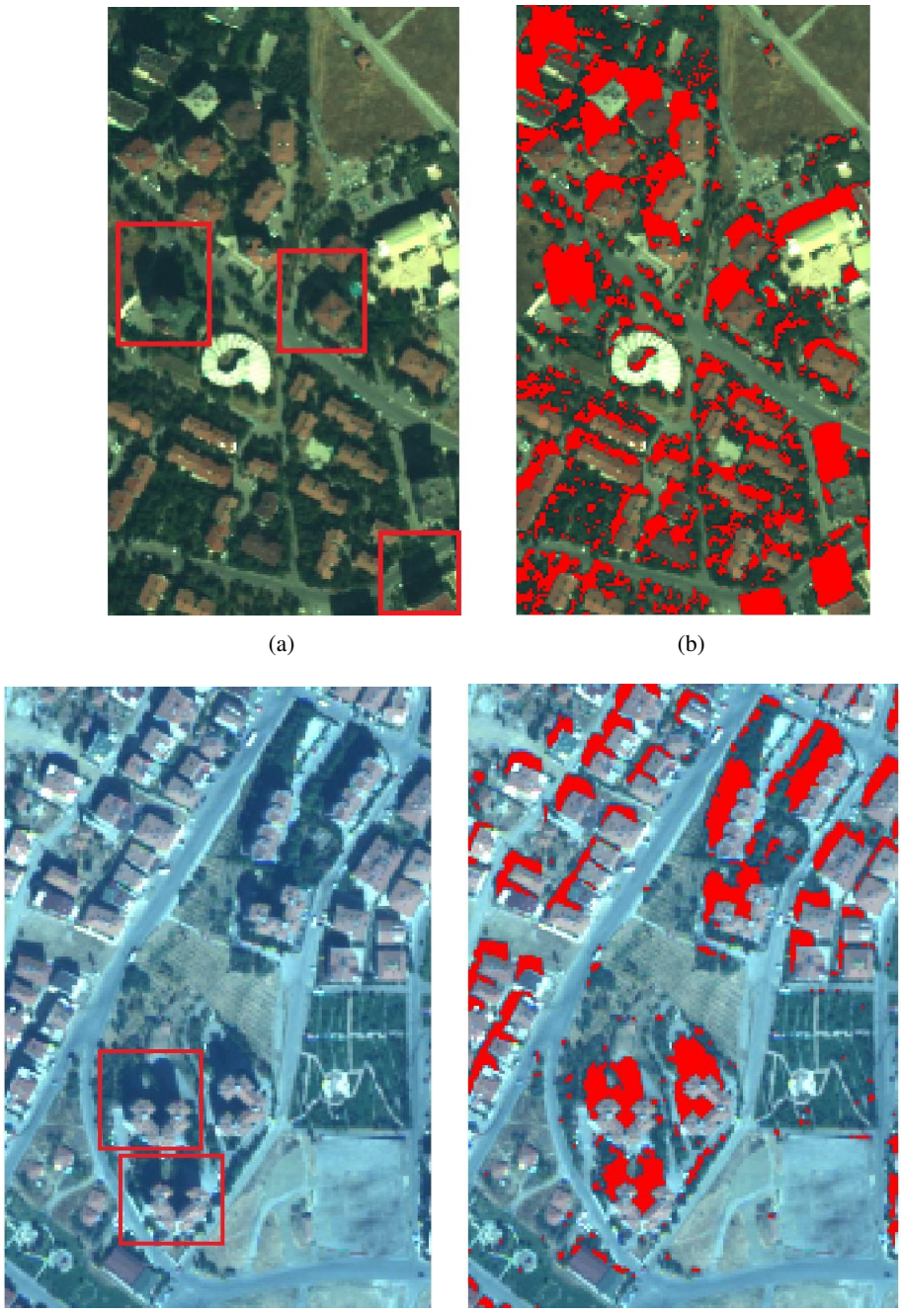

(a) (b)

(c) (d)

Figure 5.22: (a) and (c) Representation of colorful buildings (b) shadow detection of (a) (d) shadow detection of (c)

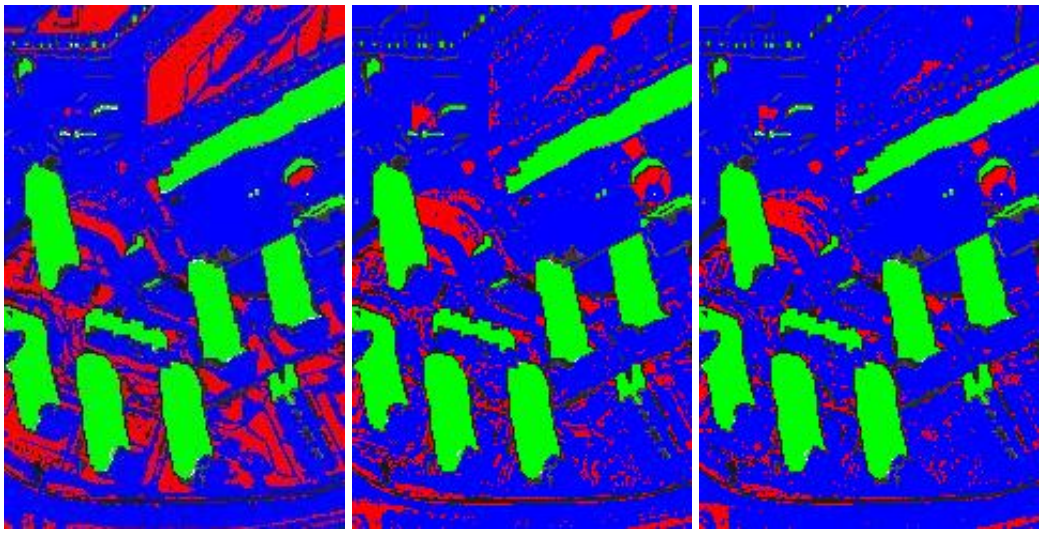

(a) (b) (c)

Figure 5.23: Result of image 1 by using method based on saturation and intensity on (a) true color image (b) false color image with NIR1 (c) false color image with NIR2

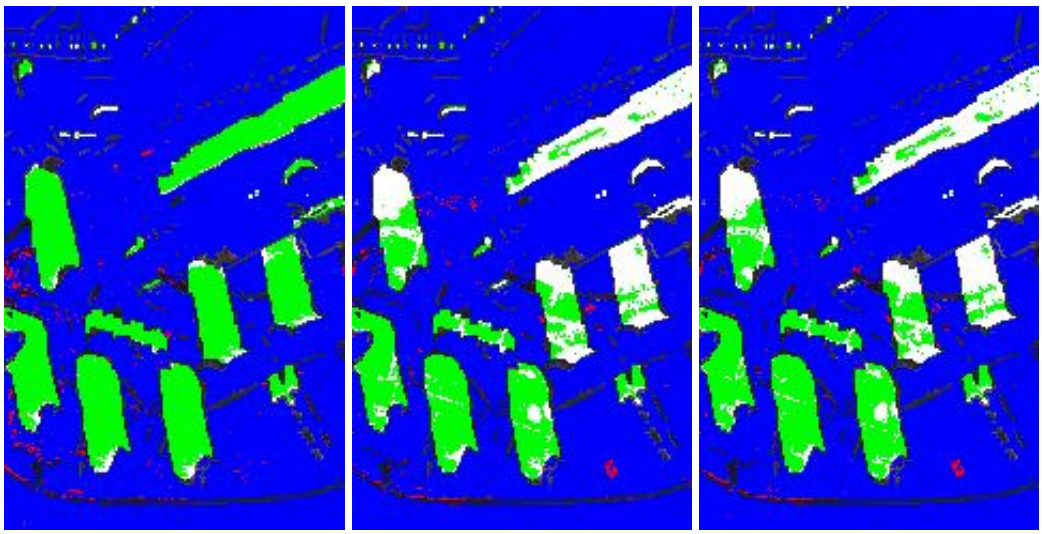

(a) (b) (c)

Figure 5.24: Result of image 1 by using method based on hue and intensity on (a) true color image (b) false color image with NIR1 (c) false color image with NIR2

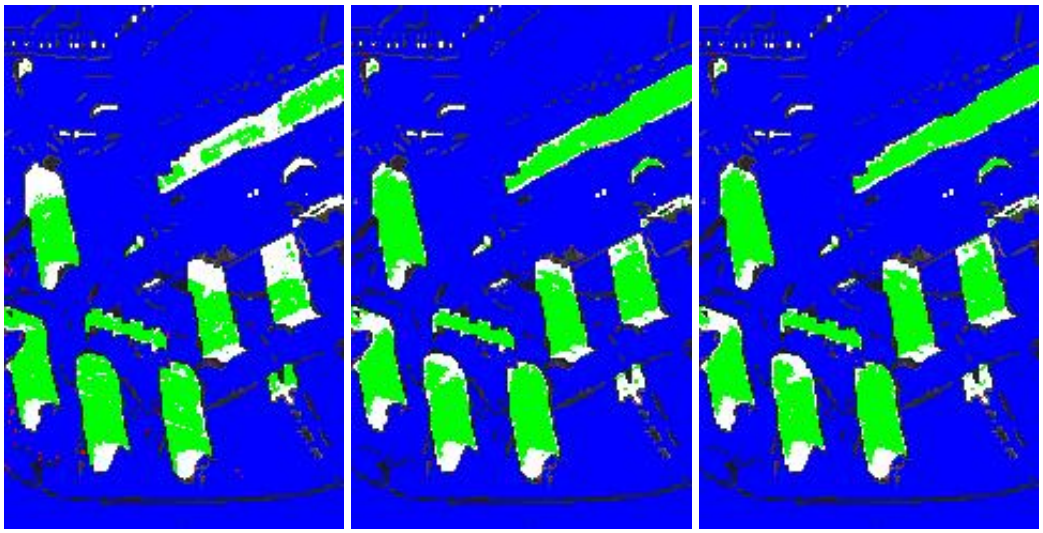

(a) (b) (c)

Figure 5.25: Result of image 1 by using method based on HCV color space on (a) true color image (b) false color image with NIR1 (c) false color image with NIR2

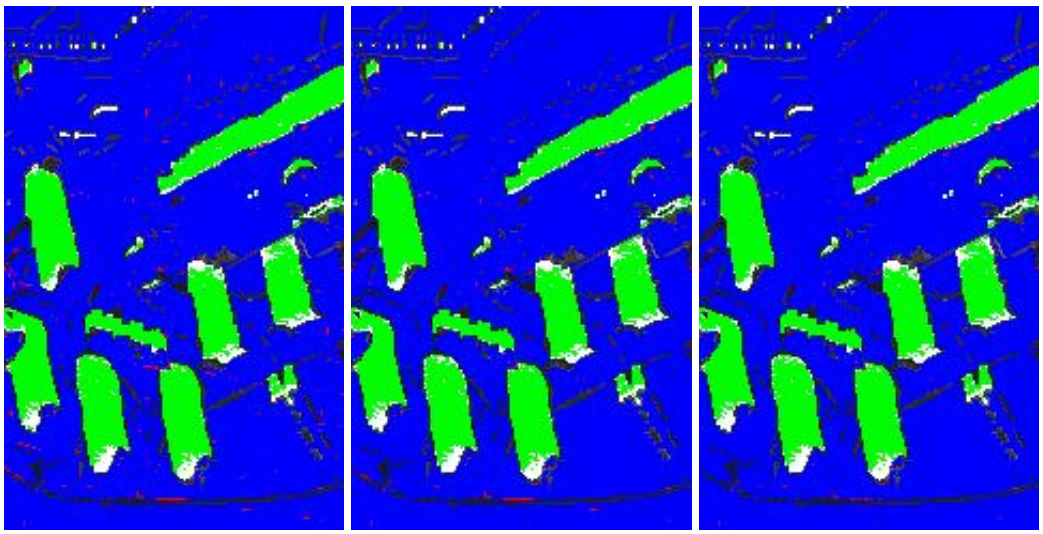

(a) (b) (c)

Figure 5.26: Result of image 1 by using method based on C_3 component on (a) true color image (b) combination of true and false color image with NIR1 (c) combination of true and false color image with NIR2

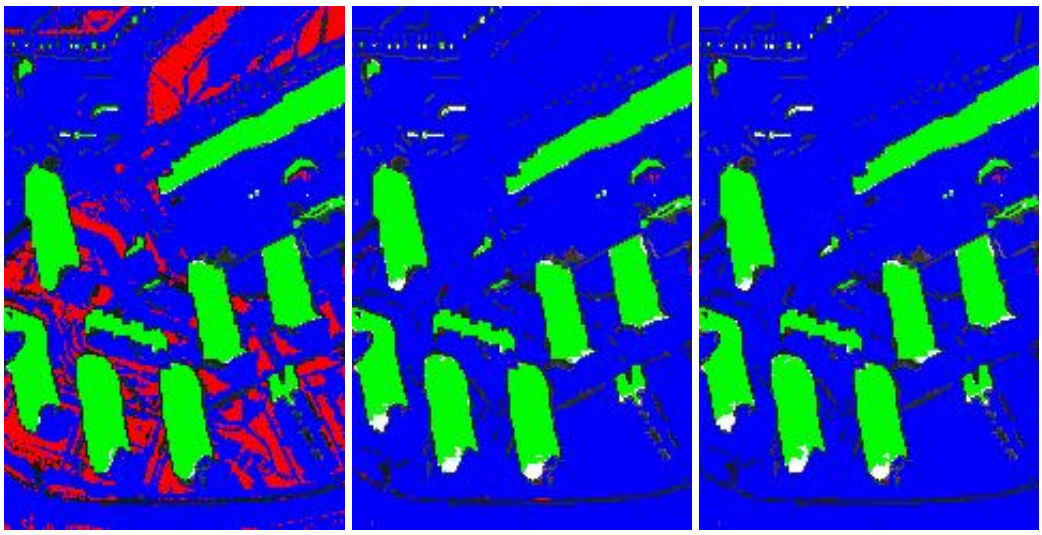

(a) (b) (c)

Figure 5.27: Result of image 1 by using method based on YUV color space (a) true color image (b) false color image with NIR1 (c) false color image with NIR2

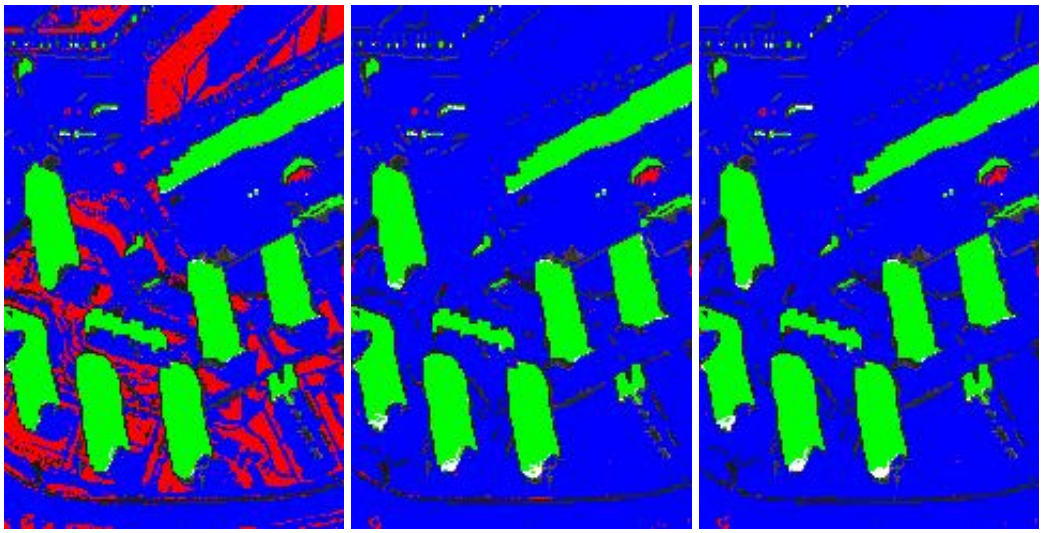

(a) (b) (c)

Figure 5.28: Result of image 1 by using method based on YC_bC_r color space (a) true color image (b) false color image with NIR1 (c) false color image with NIR2

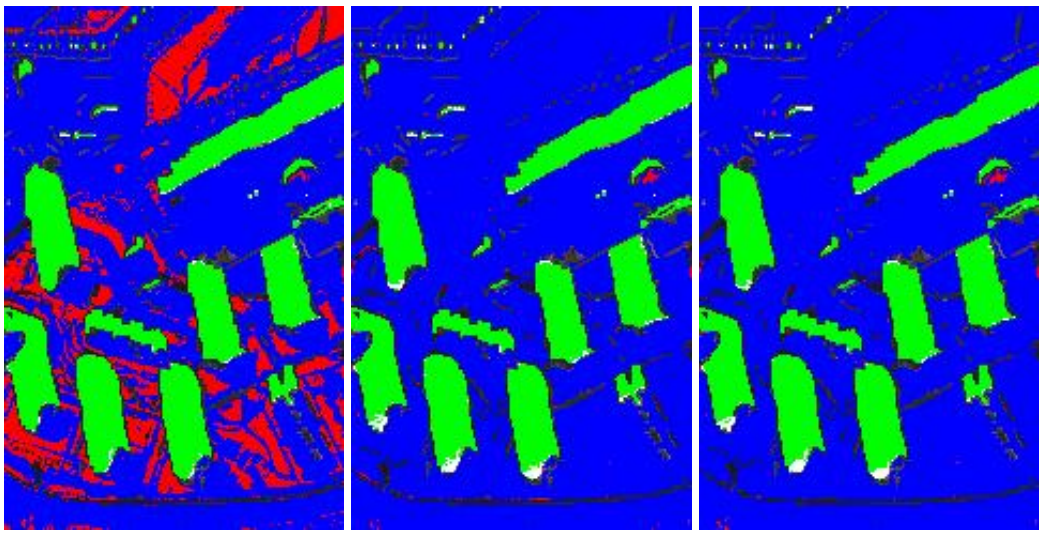

(a) (b) (c)

Figure 5.29: Result of image 1 by using method based on YIQ color space (a) true color image (b) false color image with NIR1 (c) false color image with NIR2

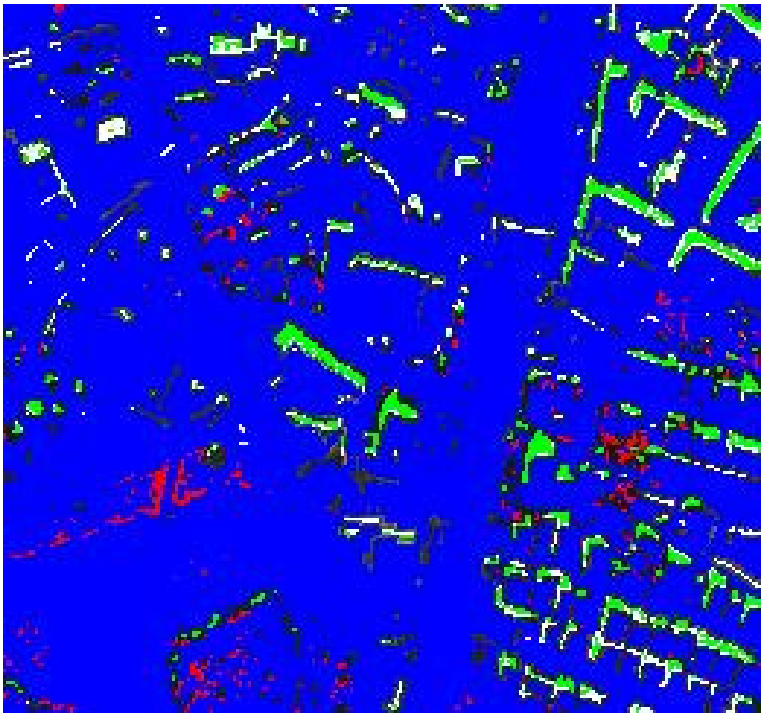

Figure 5.30: Result of image 2 by using method based on saturation and intensity on true color image

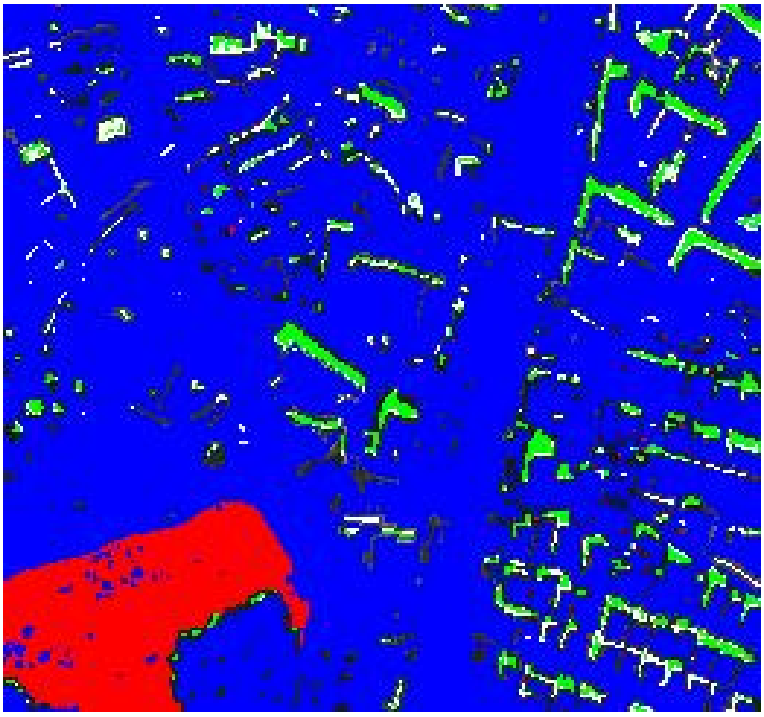

Figure 5.31: Result of image 2 by using method based on saturation and intensity on false color image with NIR1

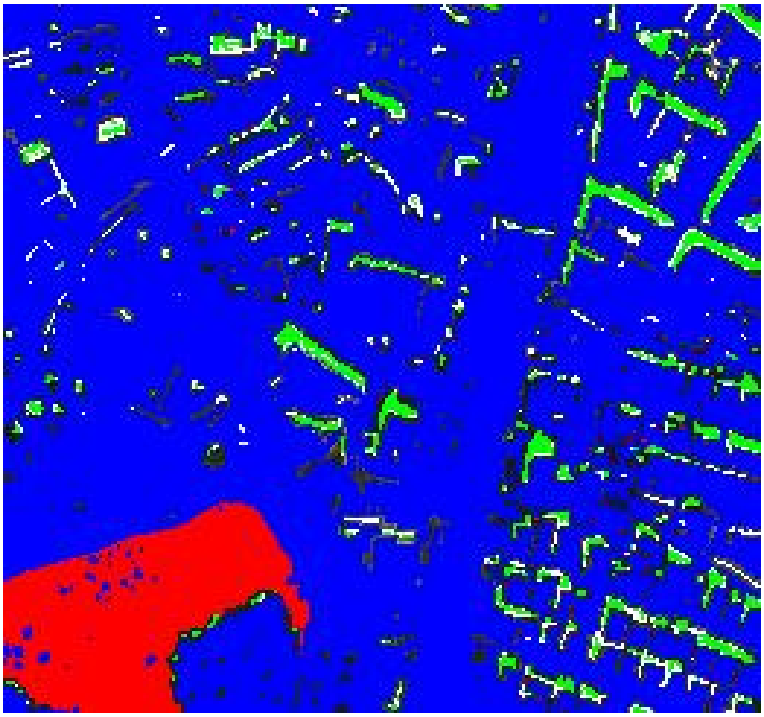

Figure 5.32: Result of image 2 by using method based on saturation and intensity on false color image with NIR2

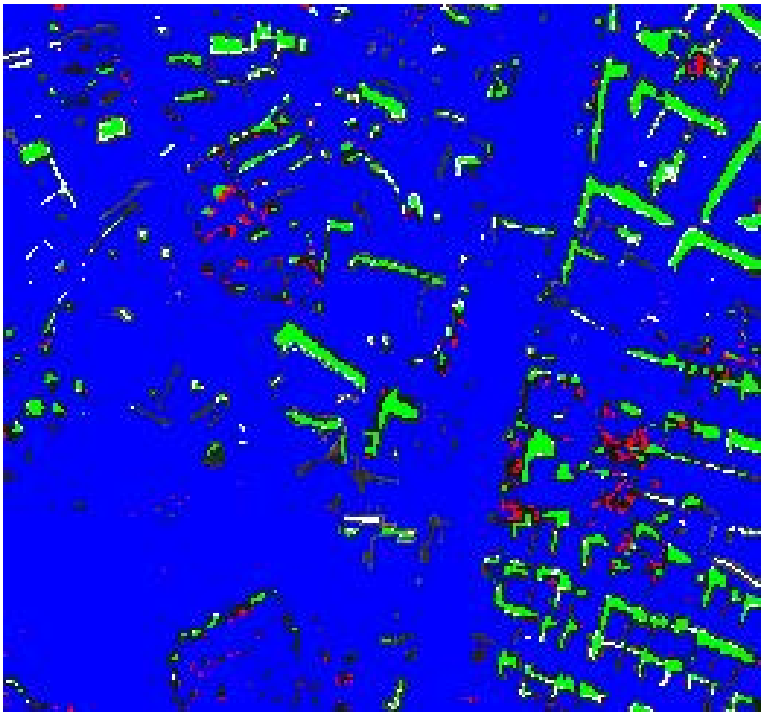

Figure 5.33: Result of image 2 by using method based on hue and intensity color space on true color image

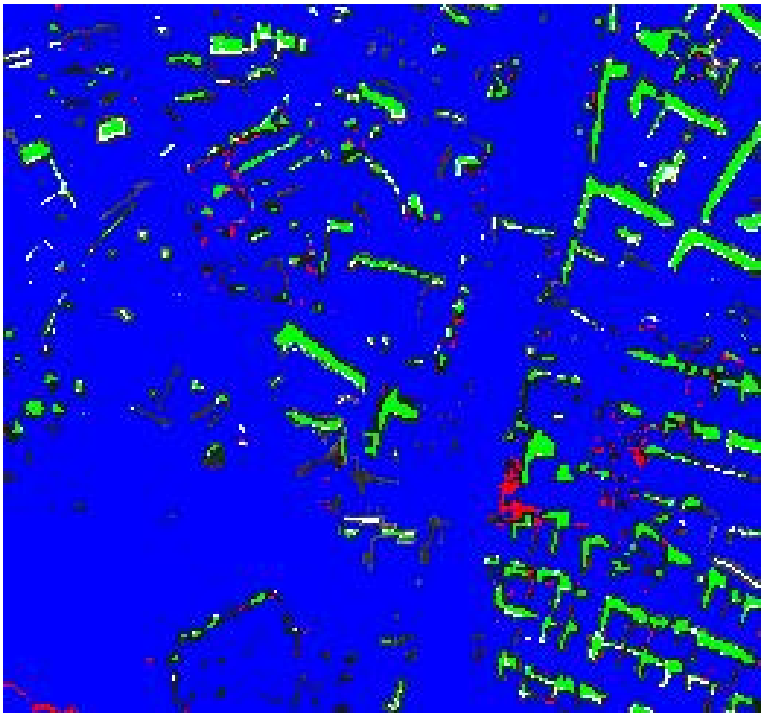

Figure 5.34: Result of image 2 by using method based on hue and intensity color space on false color image with NIR1

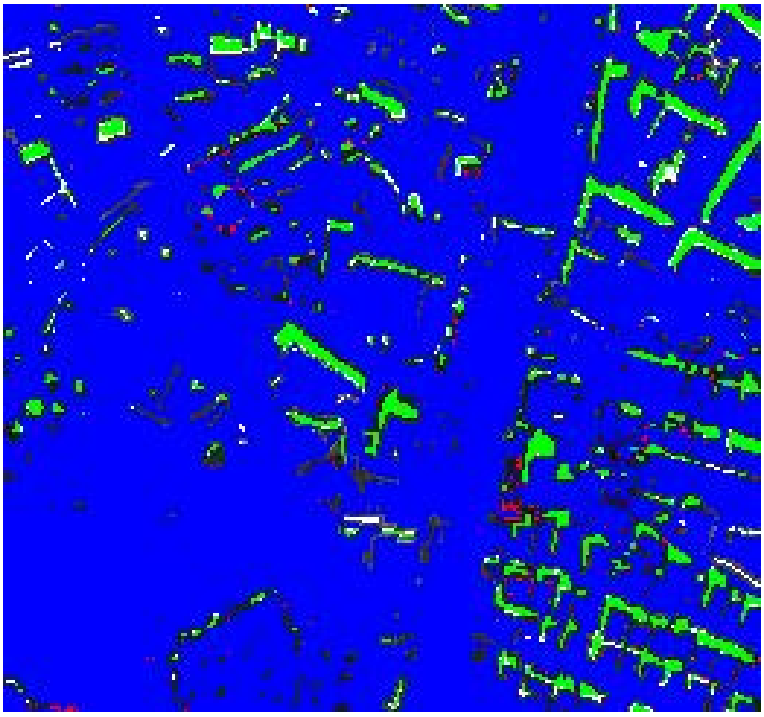

Figure 5.35: Result of image 2 by using method based on hue and intensity color space on false color image with NIR2

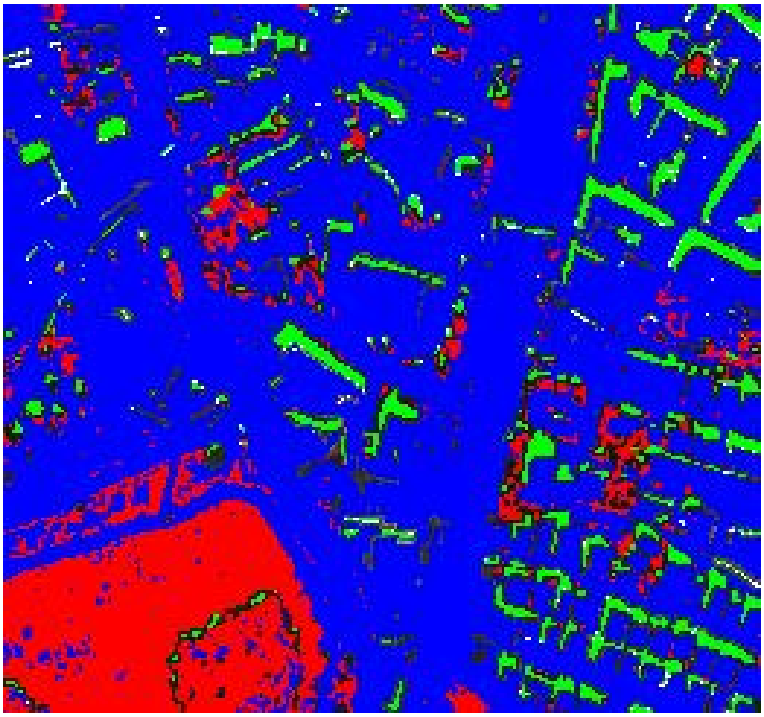

Figure 5.36: Result of image 2 by using method based on HCV color space on true color image

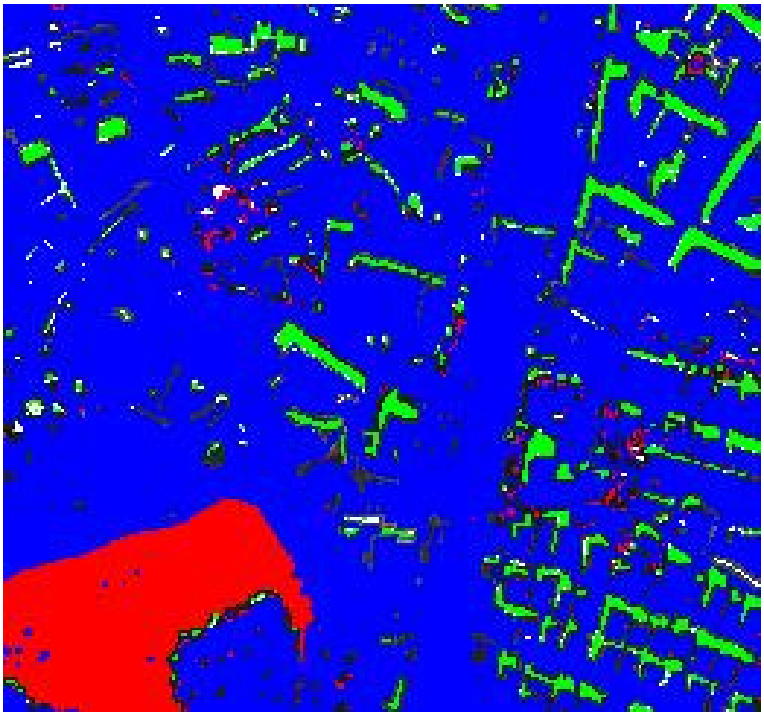

Figure 5.37: Result of image 2 by using method based on HCV color space on false color image with NIR1

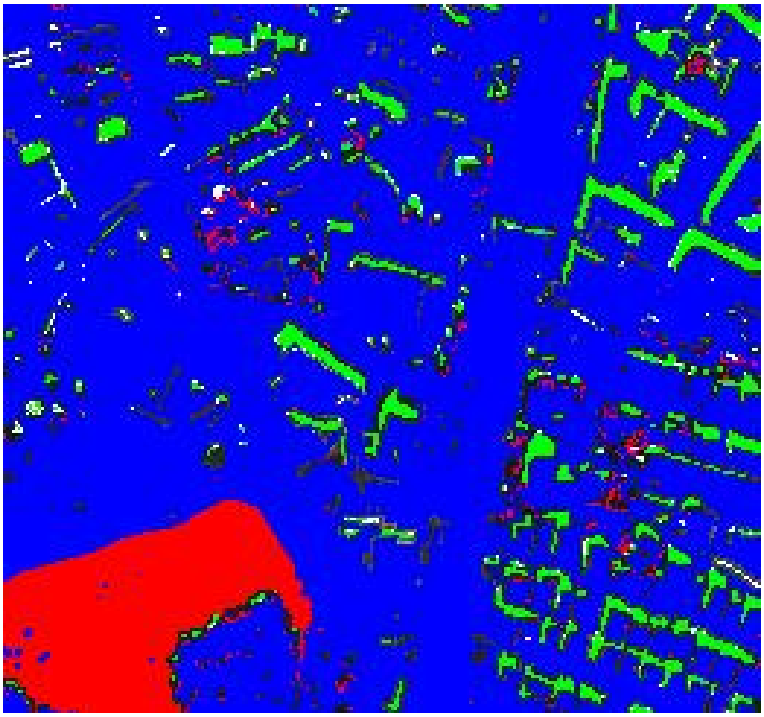

Figure 5.38: Result of image 2 by using method based on HCV color space on false color image with NIR2

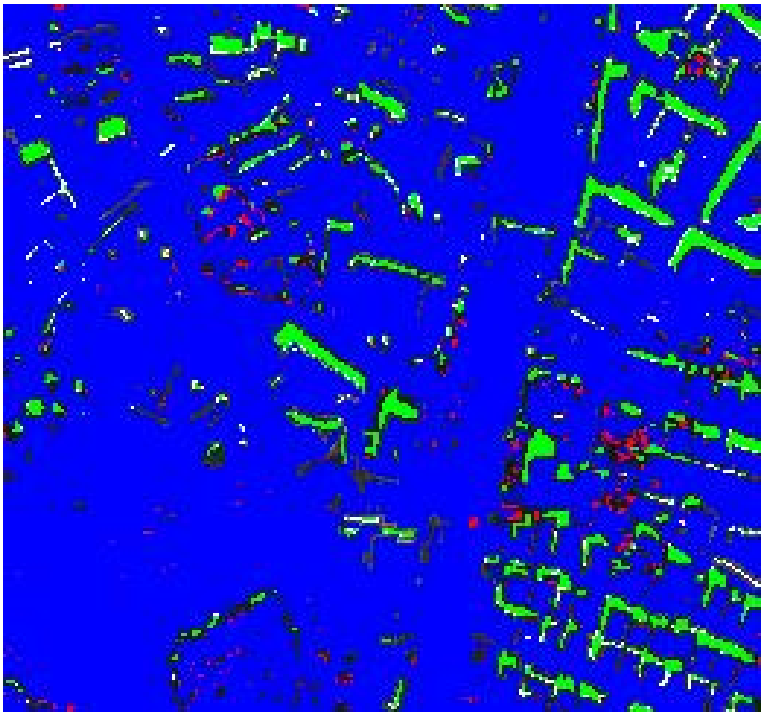

Figure 5.39: Result of image 2 by using method based on C_3 component on true color image

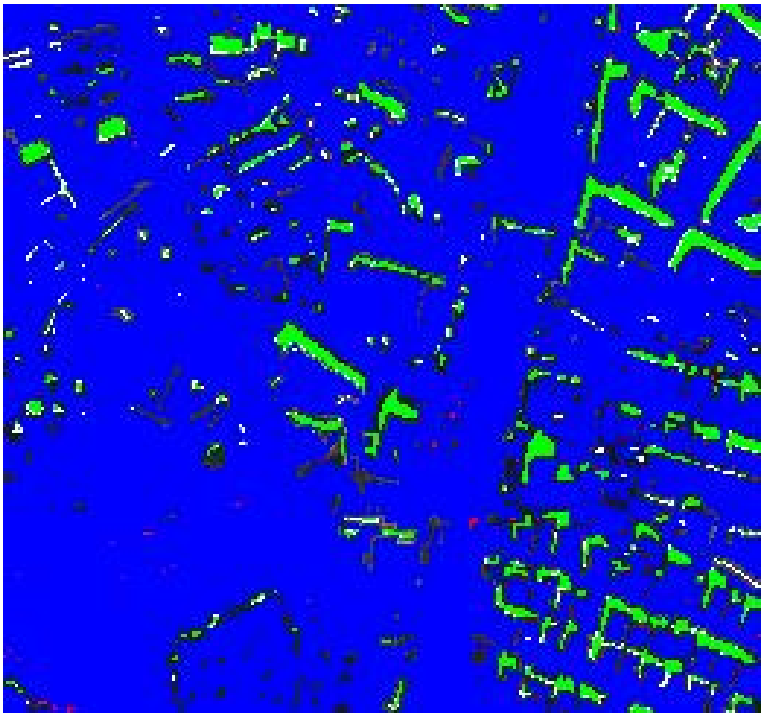

Figure 5.40: Result of image 2 by using method based on C_3 component on combination of true and false color image with NIR1

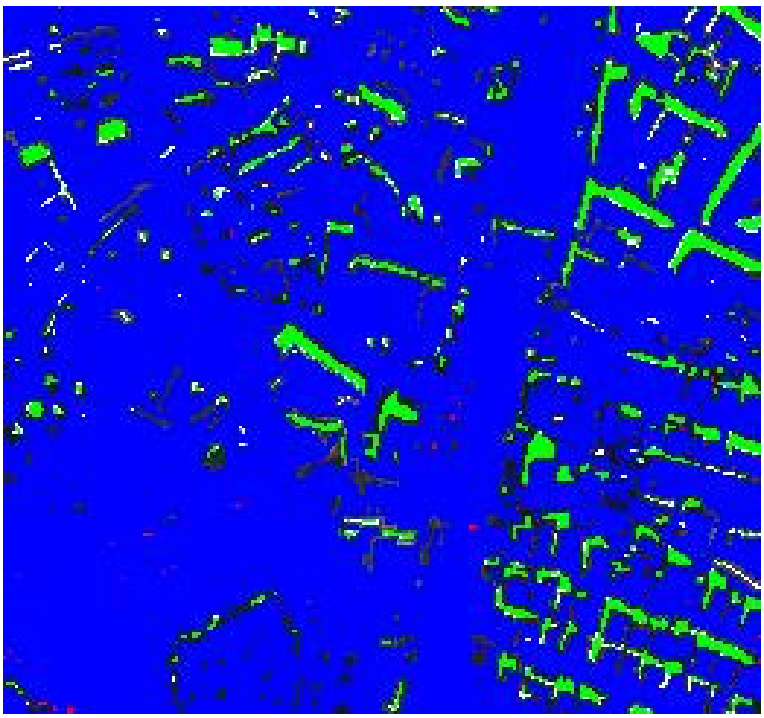

Figure 5.41: Result of image 2 by using method based on C_3 component on combination of true and false color image with NIR2

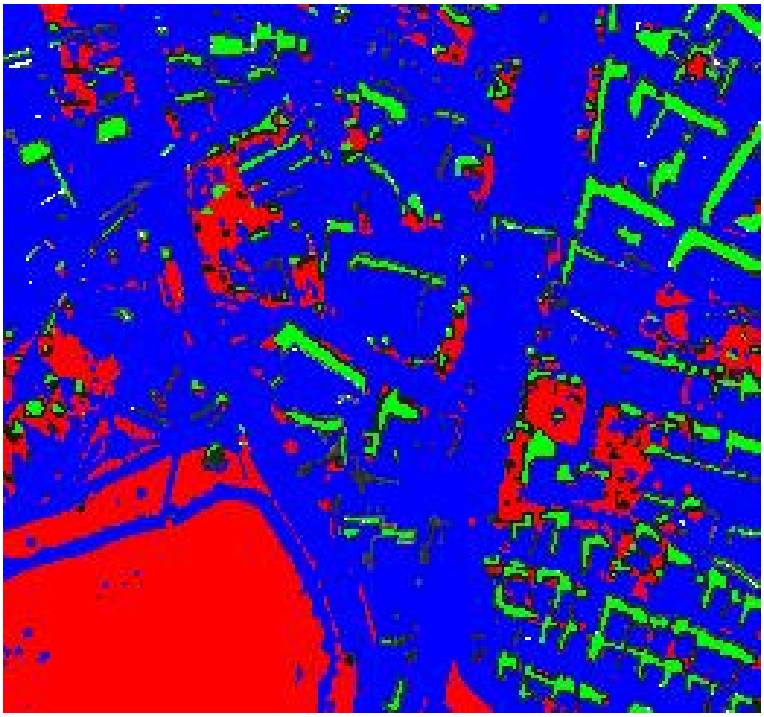

Figure 5.42: Result of image 2 by using method based on YUV color space on true color image

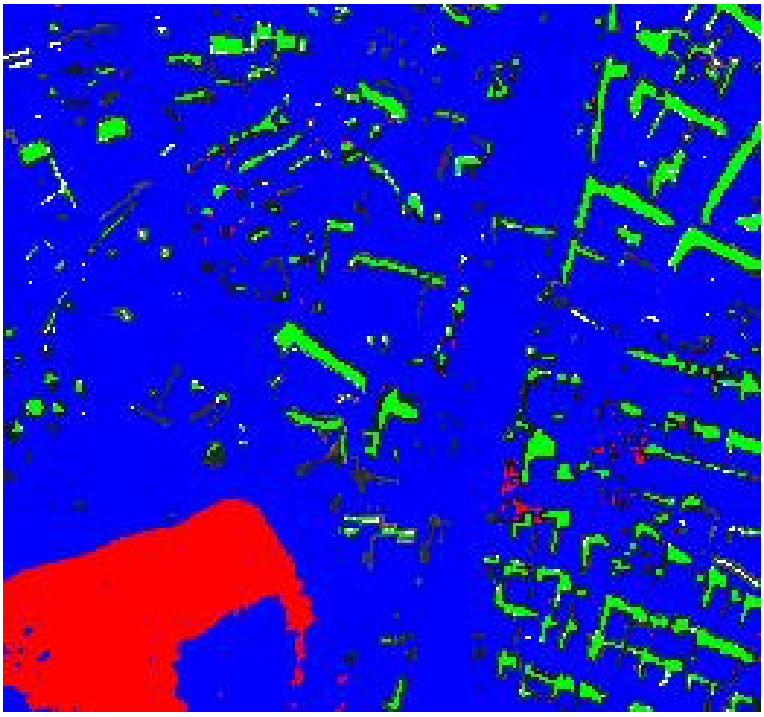

Figure 5.43: Result of image 2 by using method based on YUV color space on false color image with NIR2 band

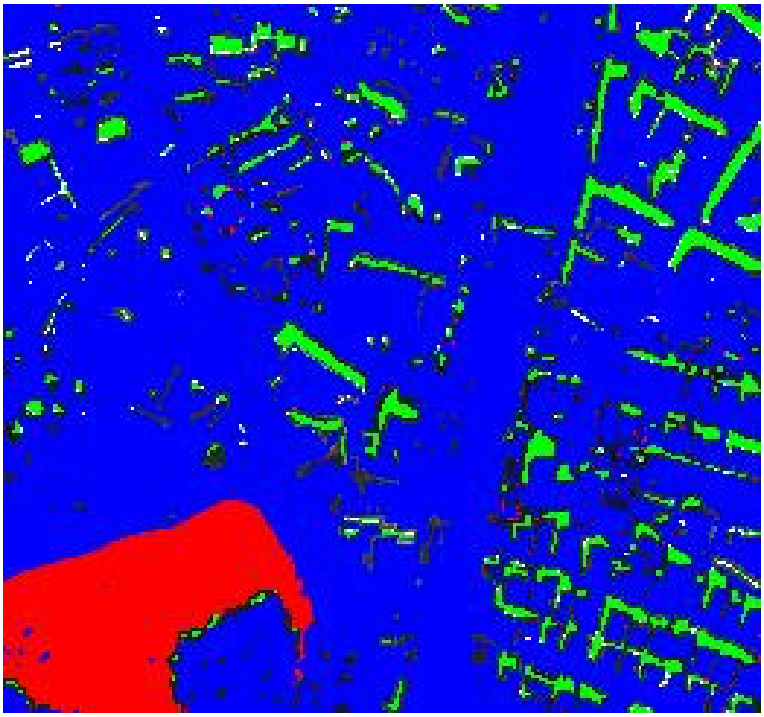

Figure 5.44: Result of image 2 by using method based on YUV color space on false color image with NIR1 band

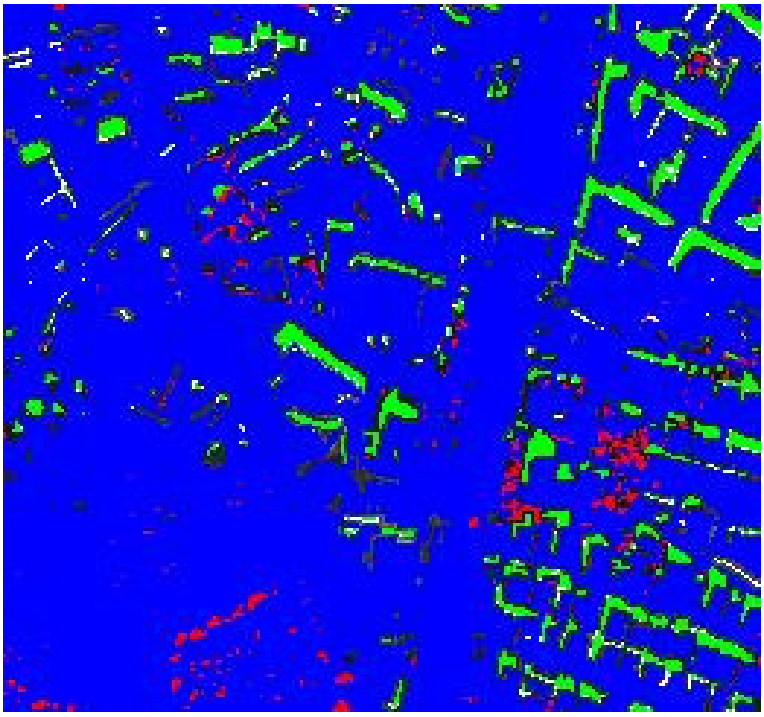

Figure 5.45: Result of image 2 by using method based on YC_bC_r color space on true color image

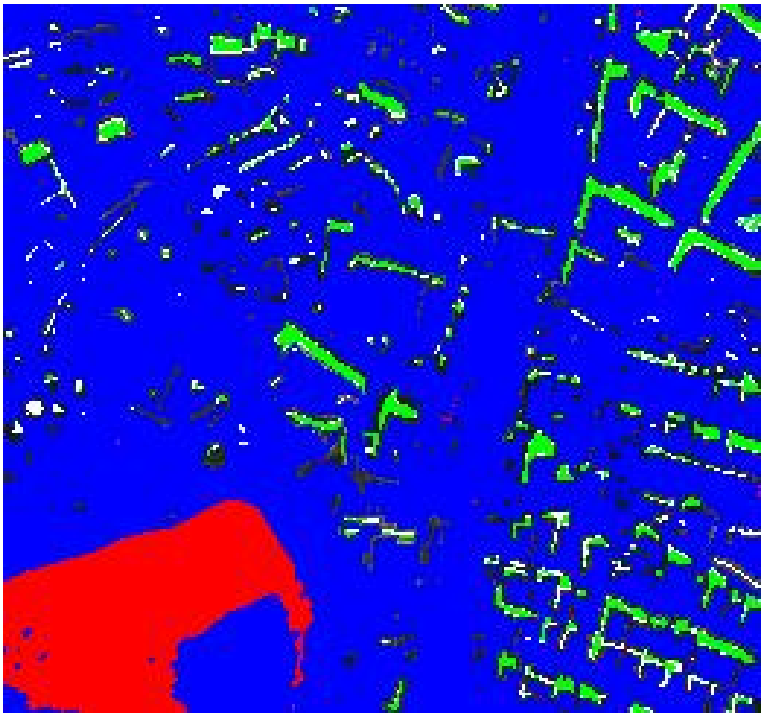

Figure 5.46: Result of image 2 by using method based on YC_bC_r color space on false color image with NIR1 band

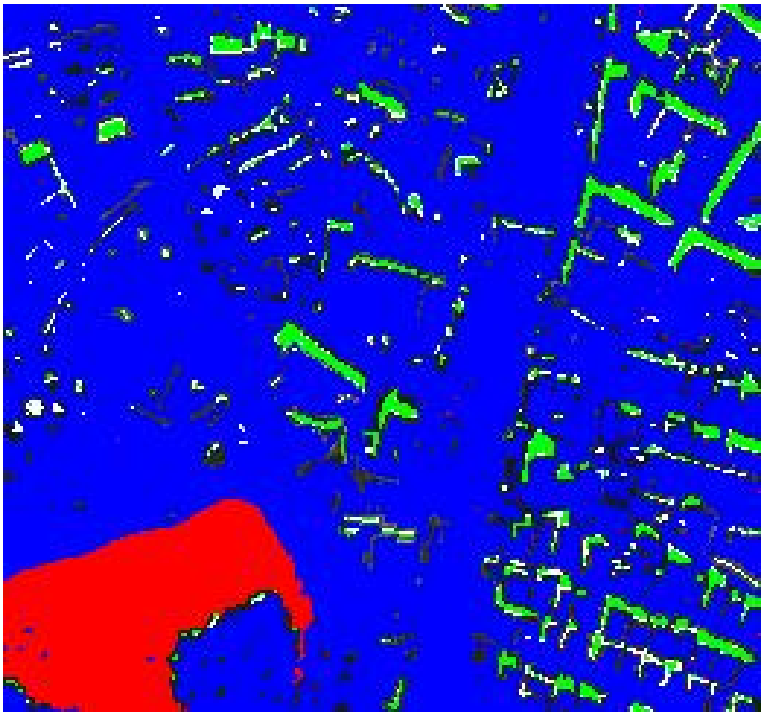

Figure 5.47: Result of image 2 by using method based on YC_bC_r color space on false color image with NIR2 band

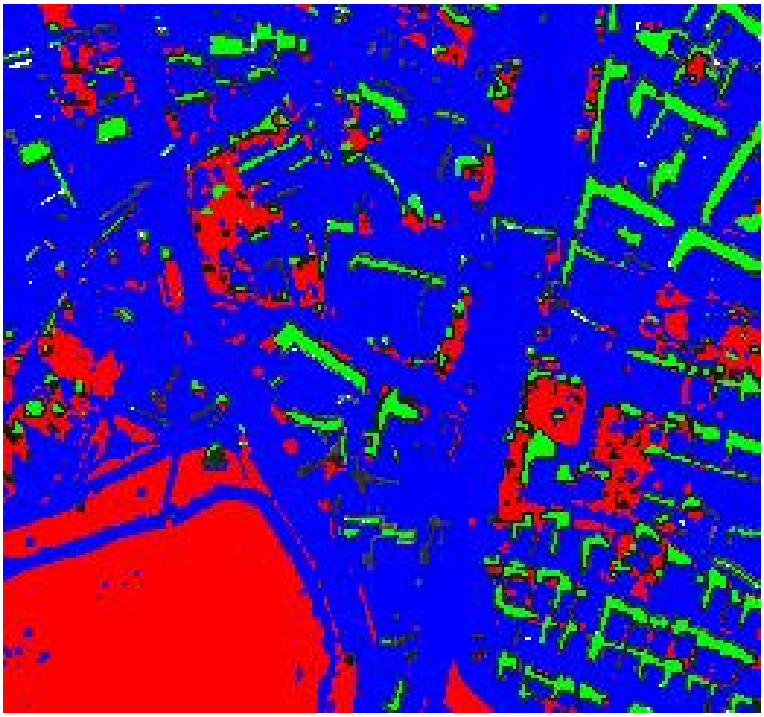

Figure 5.48: Result of image 2 by using method based on YIQ color space on true color image

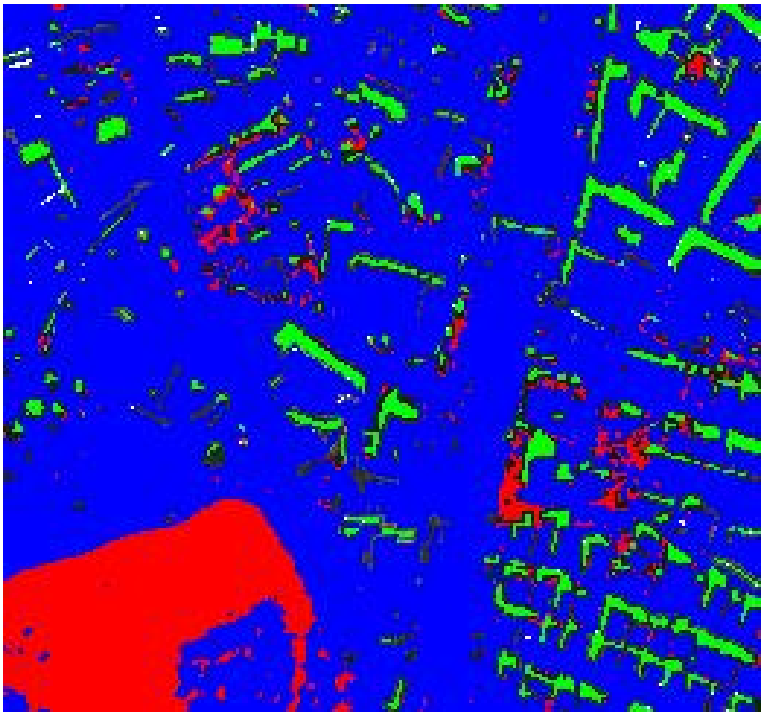

Figure 5.49: Result of image 2 by using method based on YIQ color space on false color image with NIR1 band

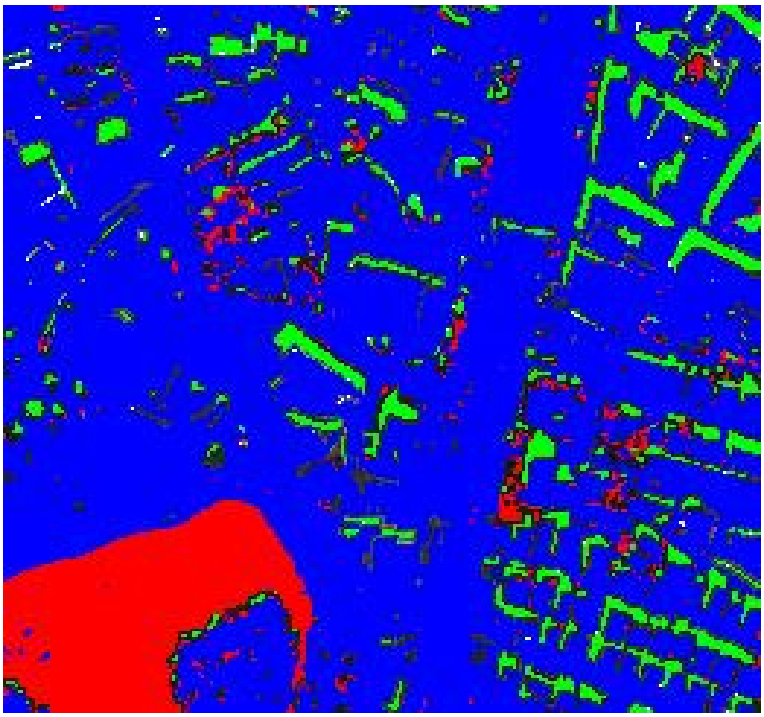

Figure 5.50: Result of image 2 by using method based on YIQ color space on false color image with NIR2 band

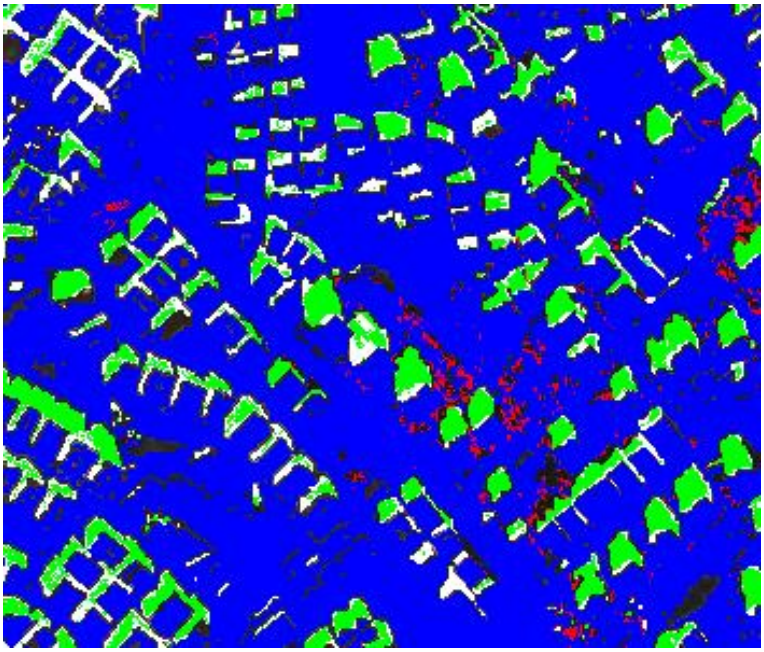

Figure 5.51: Result of image 3 by using method based on saturation and intensity on true color image

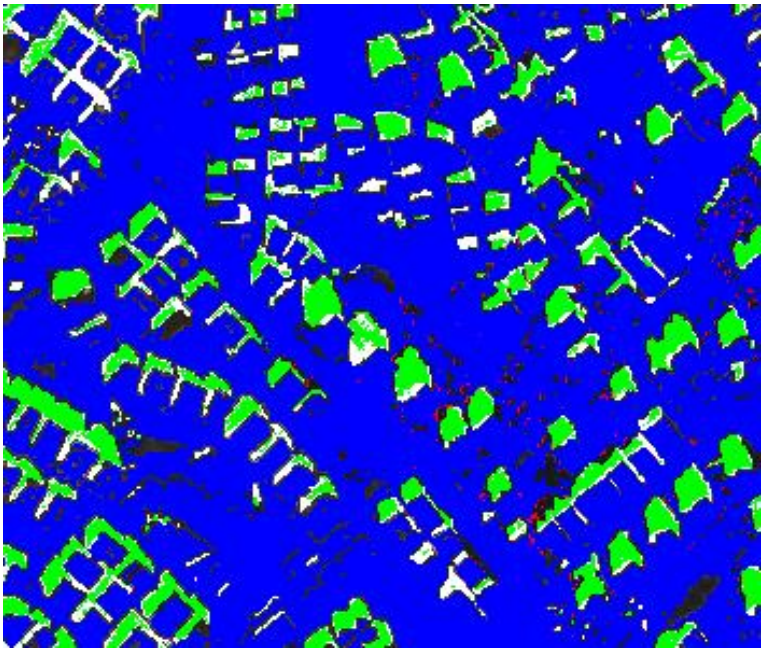

Figure 5.52: Result of image 3 by using method based on saturation and intensity on false color image with NIR1 band

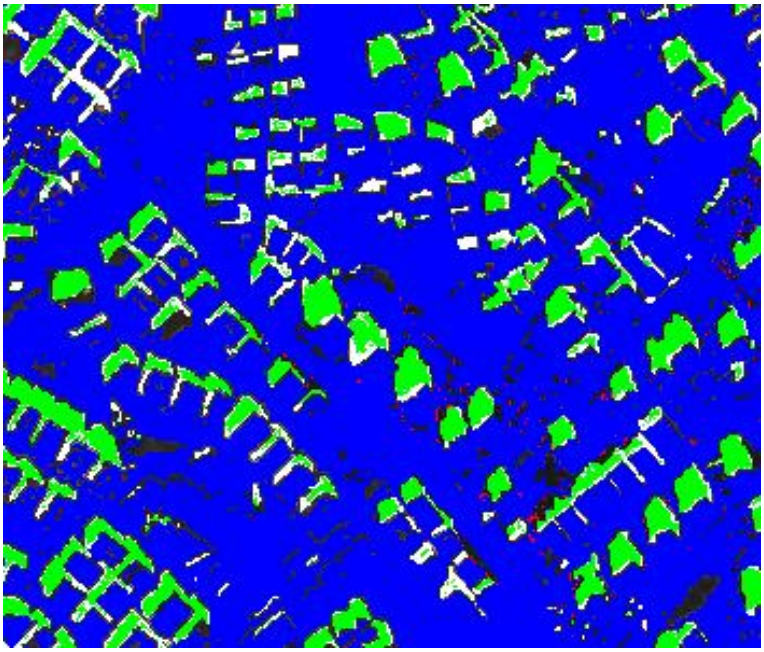

Figure 5.53: Result of image 3 by using method based on saturation and intensity on false color image with NIR2 band

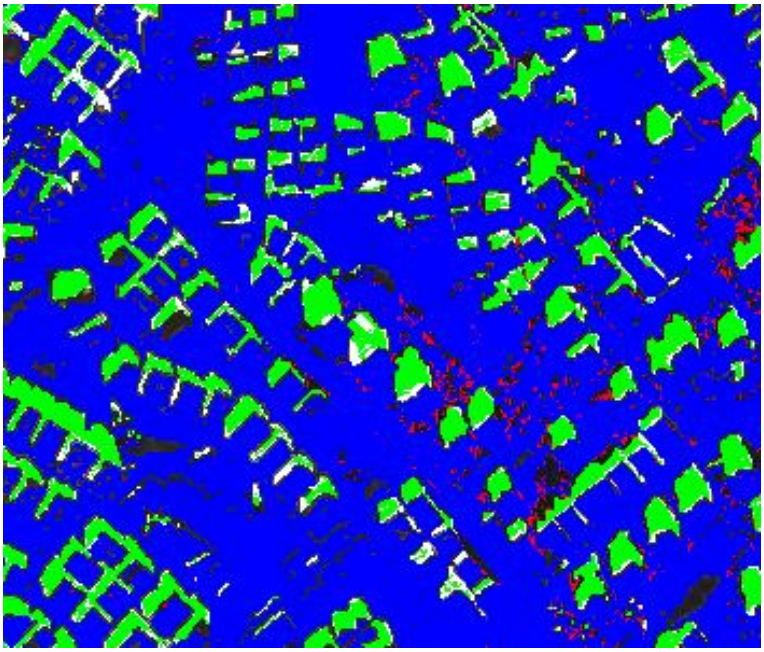

Figure 5.54: Result of image 3 by using method based on HSI color space on true color image

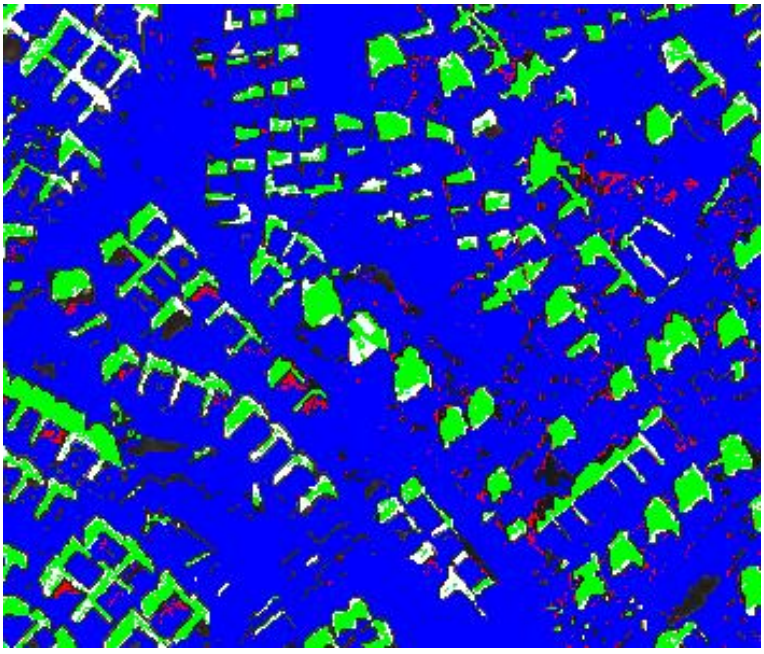

Figure 5.55: Result of image 3 by using method based on Hue and Intensity on false color image with NIR1 band

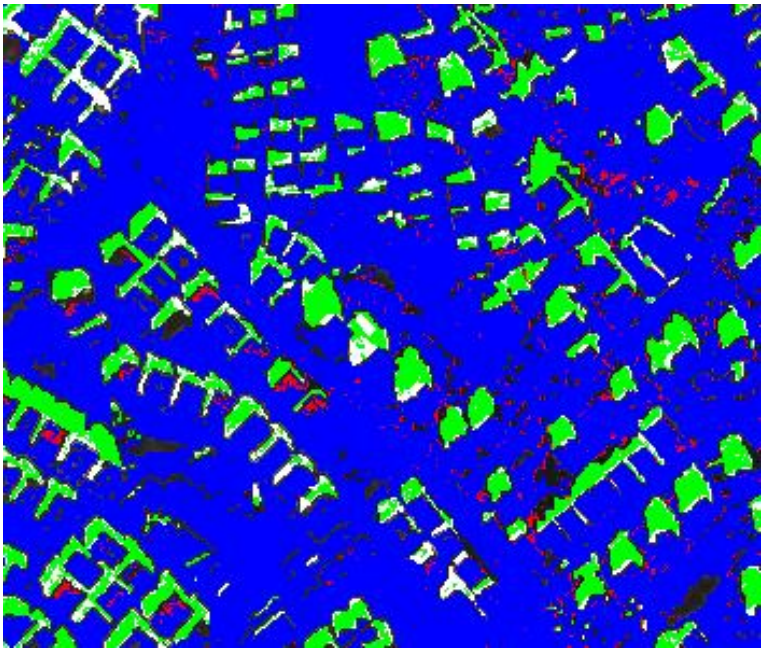

Figure 5.56: Result of image 3 by using method based on HSI color space on false color image with NIR2 band

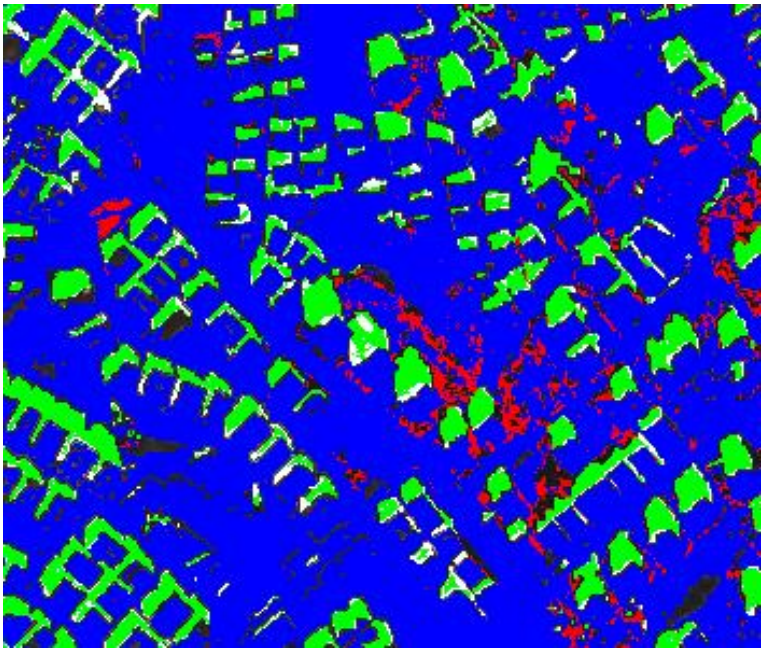

Figure 5.57: Result of image 3 by using method based on HCV color space on true color image

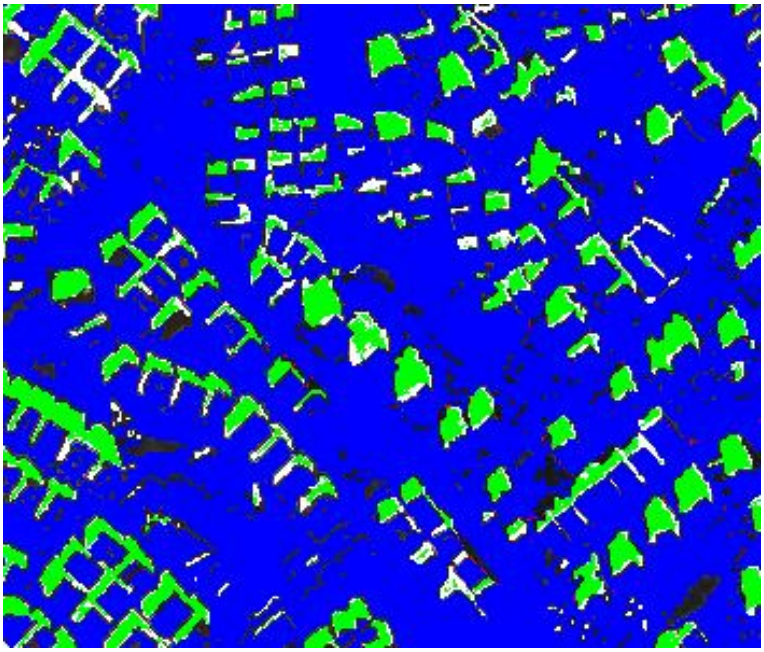

Figure 5.58: Result of image 3 by using method based on HCV color space on false color image with NIR1 band

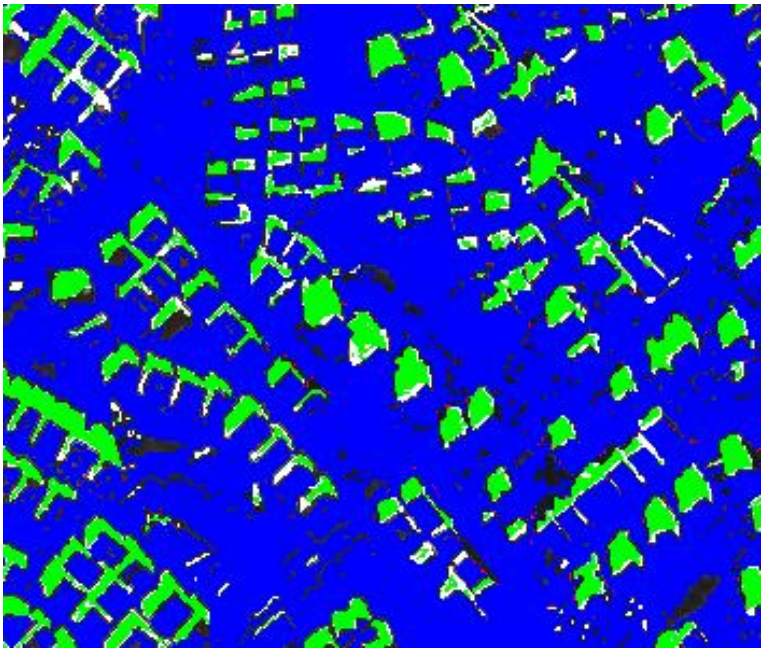

Figure 5.59: Result of image 3 by using method based on HCV color space on false color image with NIR2 band

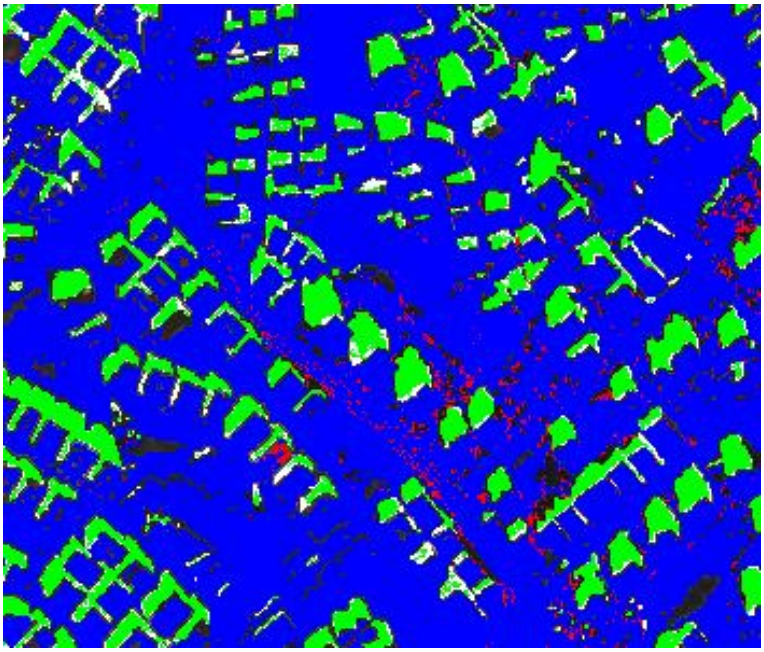

Figure 5.60: Result of image 3 by using method based on C_3 component on true color image

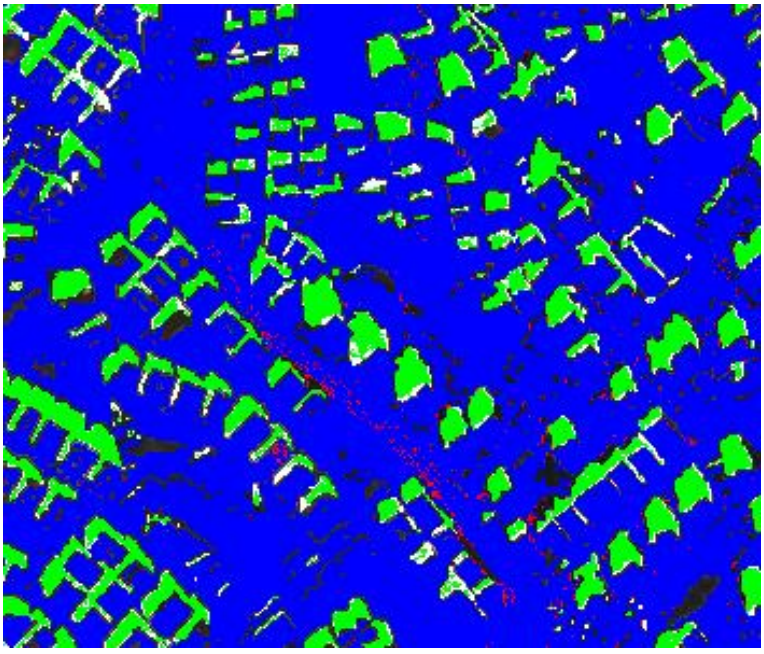

Figure 5.61: Result of image 3 by using method based on C_3 component on combination of true and false color image with NIR1 band

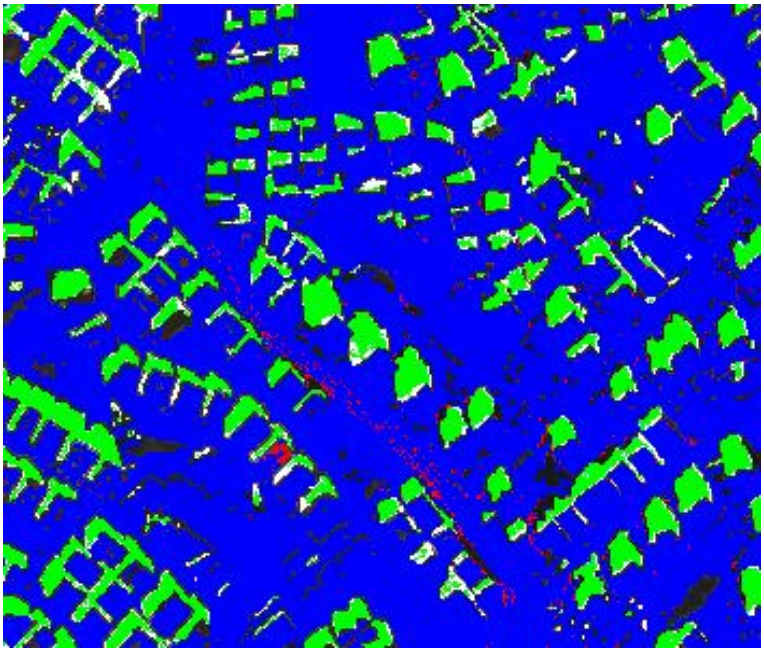

Figure 5.62: Result of image 3 by using method based on C_3 component on combination of true and false color image with NIR2 band

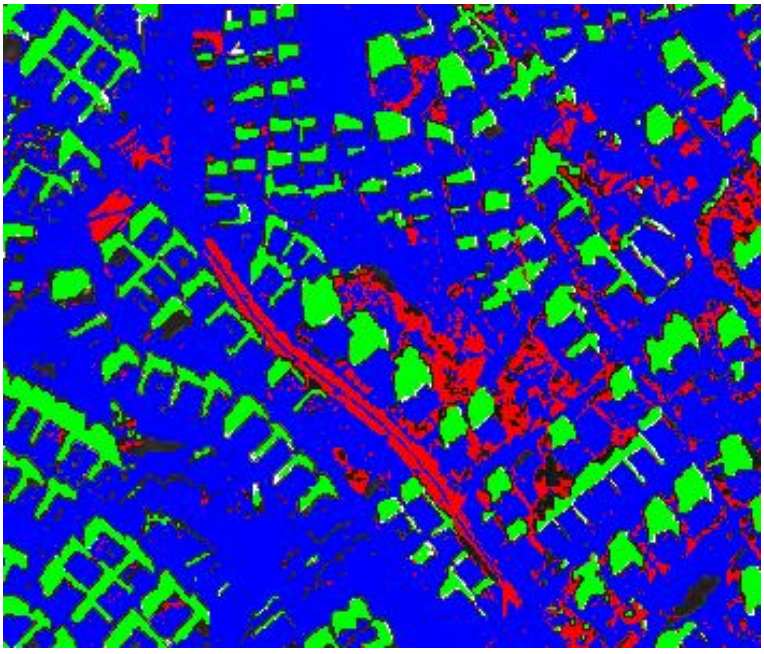

Figure 5.63: Result of image 3 by using method based on YUV color space on true color image

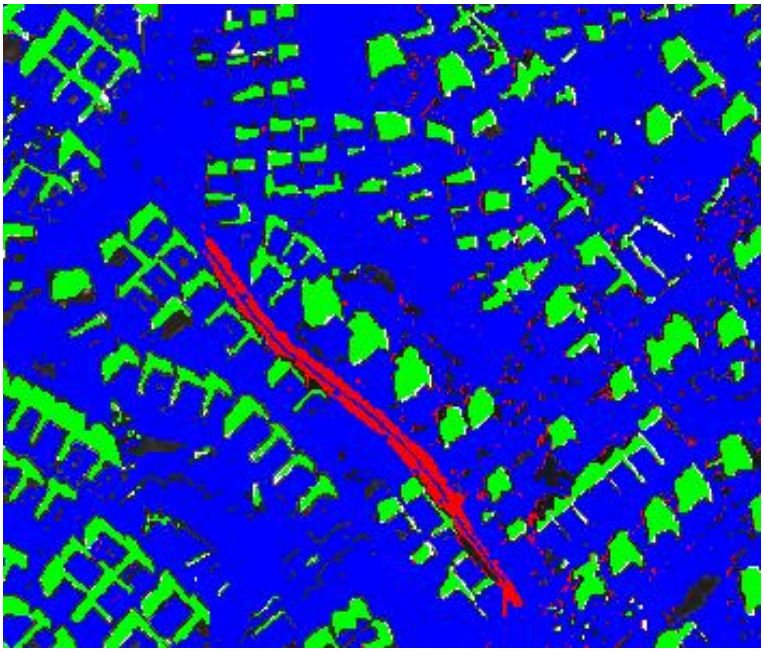

Figure 5.64: Result of image 3 by using method based on YUV color space on false color image with NIR1 band

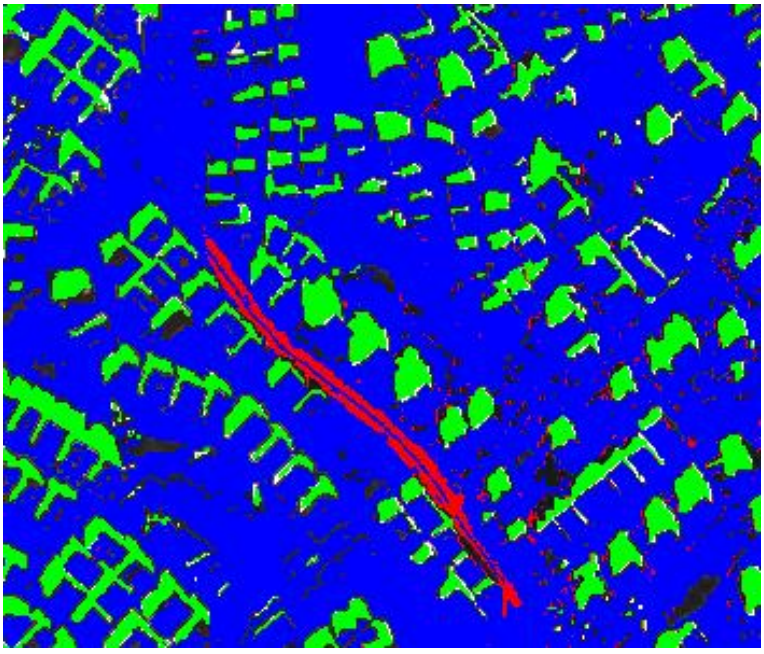

Figure 5.65: Result of image 3 by using method based on YUV color space on false color image with NIR2 band

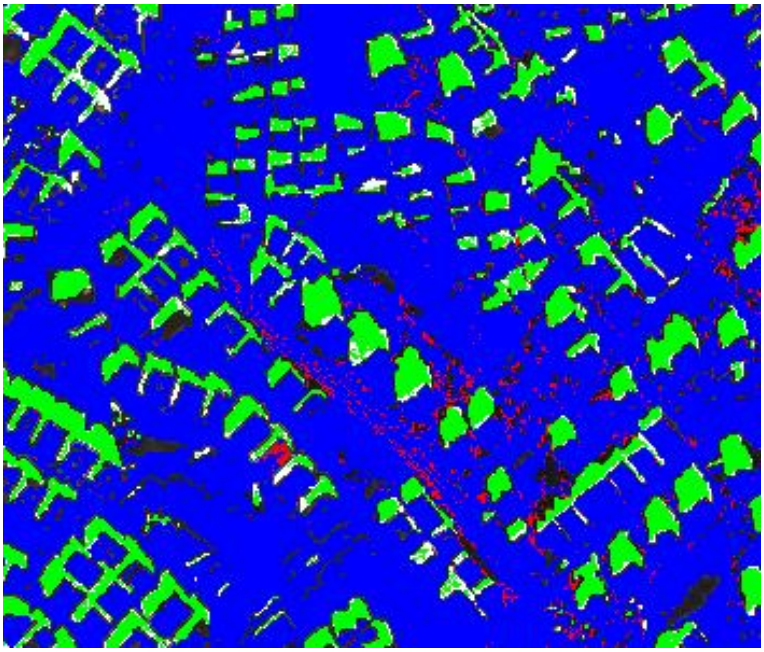

Figure 5.66: Result of image 3 by using method based on YC_bC_r color space on true color image

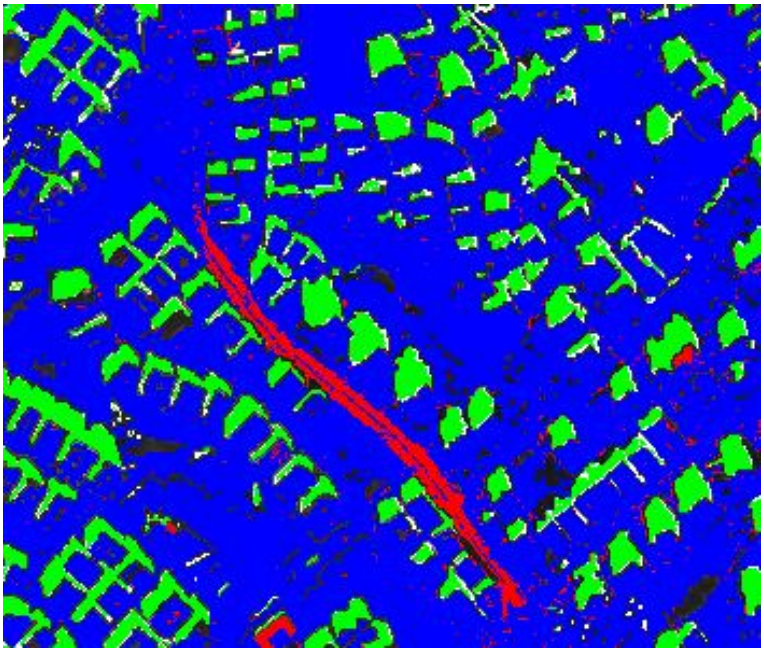

Figure 5.67: Result of image 3 by using method based on YC_bC_r color space on false color image with NIR1 band

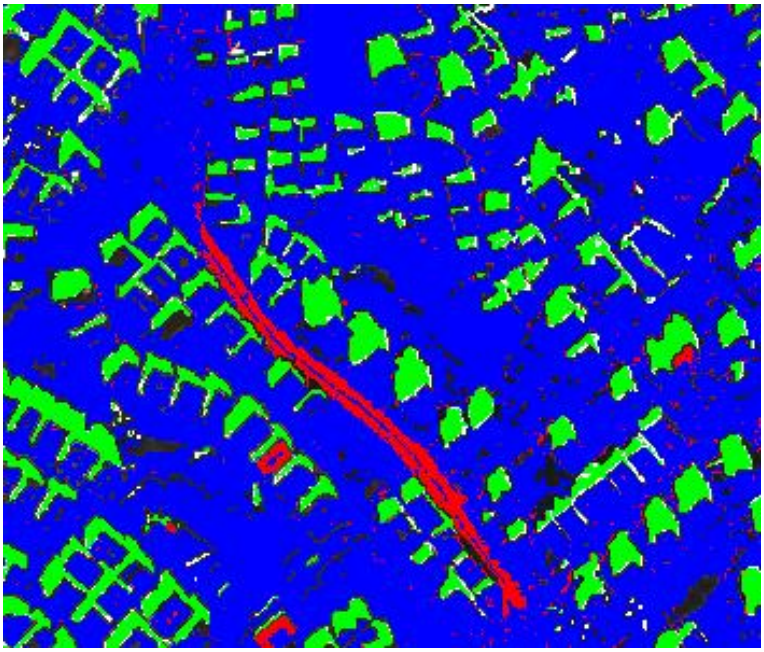

Figure 5.68: Result of image 3 by using method based on YC_bC_r color space on false color image with NIR2 band

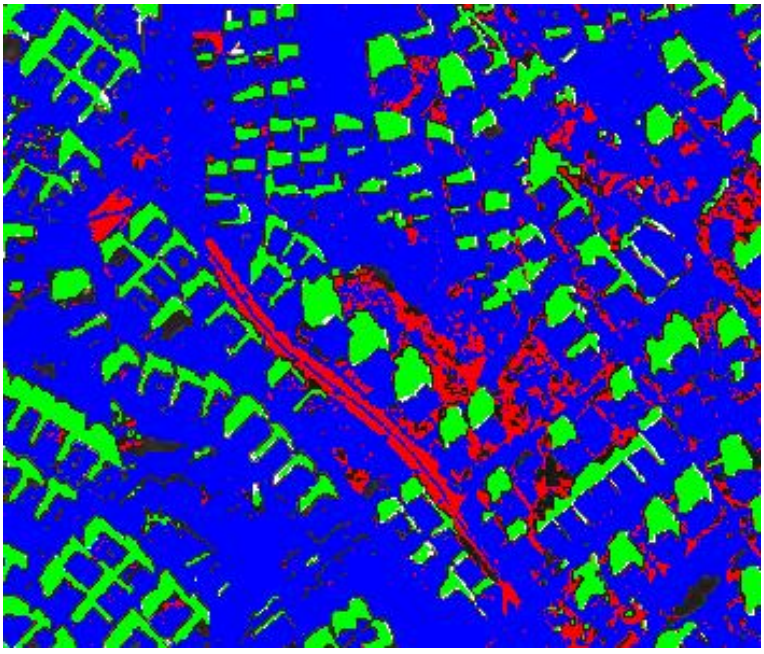

Figure 5.69: Result of image 3 by using method based on YIQ color space on true color image

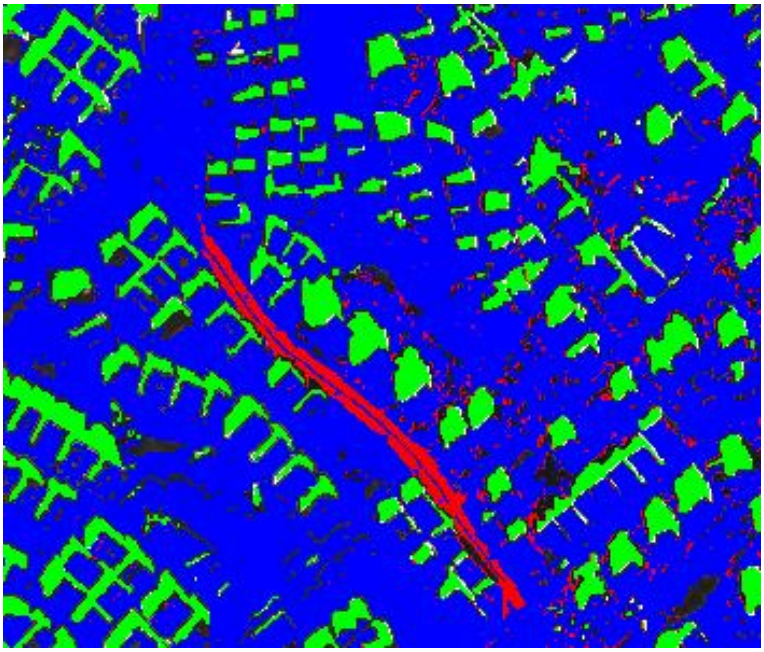

Figure 5.70: Result of image 3 by using method based on YIQ color space on false color image with NIR1 band

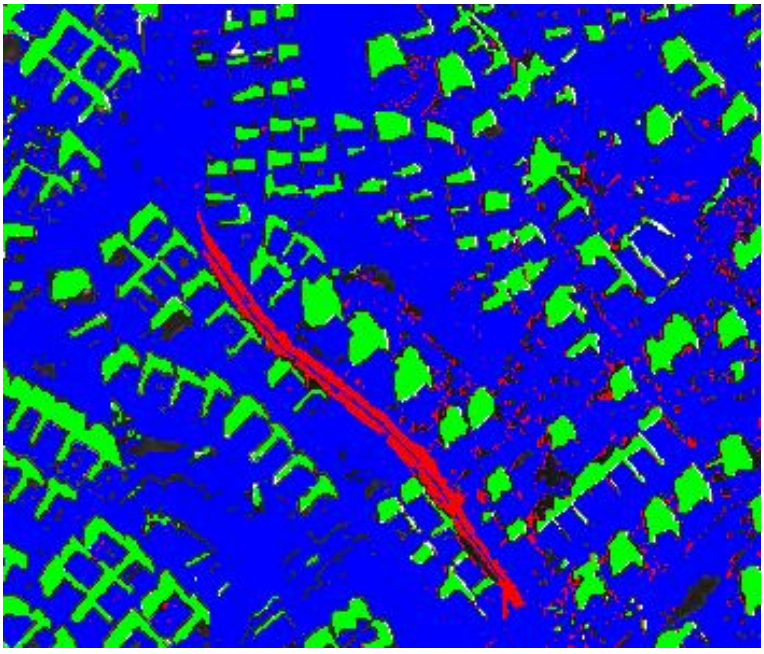

Figure 5.71: Result of image 3 by using method based on YIQ color space on false color image with NIR2 band

CHAPTER 6

CONCLUSION

In this thesis, new methods are proposed to detect shadows automatically in multispectral images. These methods are based on histogram thresholding to proposed new ratios. Each ratio is obtained by using different color spaces. The conversion to color spaces is applied to not only standard 3-band RGB images but also a combination of 3 bands and one of the combination bands is one of two Worldview-2 bands corresponding to NIR band wavelength range. As a result, NIR band which has bigger changes between shadow and non-shadow region than red, green and blue bands is utilized.

Shadows have high hue and saturation value while intensity values are lower in shadow region. At the same time, blue band value is usually higher than red and green bands' values and the other biggest value is close to blue band value in shadow region. Thus, C_3 component of $C_1C_2C_3$ space is highest value in shadow region. In the light of these information, some ratios are suggested in the literature. We are added NIR band to C_3 component to eliminate vegetation pixels because vegetation pixels have high NIR band value and vegetation is detected as shadows. Besides, in the color spaces based on luminance and chroma, luminance has higher values in shadow region than non-shadow region whereas one of the chroma components has lower values. Therefore, the ratios which are appropriate for these properties are proposed. All of the ratios are applied both standard RGB images and false color images which consist of Red, Green and NIR bands.

One of the most important properties of proposed methods is that they are fully automatic method to detect shadows. In some similar methods in the literature [37], [25], [10], [4], threshold point is selected manually or automatic threshold point is distant from optimal threshold point. In our methods, Otsu thresholding is applied. However, while in the literature Otsu thresholding is applied once, we propose to apply Otsu thresholding twice to data in some ratios which separate the pixels more than two classes. The first threshold separates the data into two classes which have maximum variance difference, whereas second threshold separates shadows from non-shadow region.

The dataset obtained by WorldView-2 satellite sensor is used to test the methods. The methods are applied to three remote sensing images . One image includes lake water, whereas another has swimming pool. These images have 8 bands and one of them, NIR2 is a new band which is in higher wavelength range. Therefore, the false color images are created with both NIR1 and NIR2 bands.

The algorithms results can be summarized as given below:

- On average, the most successful results are taken with new proposed C_3 component. Although, many algorithms detect water as shadow, the combination of C_3 and C_3' does not detect water pixels as shadows.
- If the water pixels are not contained in the image, the ratios based on luminance and chroma give the most successful results.
- False color images are more helpful than true color images except the ratios based on hue and intensity and YC_bC_r.
- When NIR2 band is used for false color images, the results are closer to groundtruth maps. Therefore, new NIR band of Worldview-2 contributes to the better results on shadow detection.
- However, these ratios can not detect self-shadow pixels if the self-shadow is on the white surface. Therefore, self-shadow detection depends on the surface color.

6.1 Future Works

As future works, shadow detection algorithms could be studied on hyperspectral images. Since hyperspectral images give more detailed information than multispectral images, better results may be obtained in shadow detection.

Determining the threshold point affects the success of our algorithms. We proposed to apply Otsu thresholding twice for some ratios. However, another method could be used to obtain better results.

Shadows help to find solution to the classification and change detection problems. However, shadow detection is not sufficient to overcome these problems. Modified radiometric information of the materials on shadows must be turned to the original values and so shadows must be removed. Thus, objects can be classified correctly and changes can be focused on change detection problems.

Inference of 3D information of the objects can be obtained shadow detection. After we use our algorithms to detect shadows, building height estimation problems can be studied.

REFERENCES

[1] K. Adeline, M. Chen, X. Briottet, S. Pang, and N. Paparoditis. Shadow detection in very high spatial resolution aerial images: A comparative study. *{ISPRS} Journal of Photogrammetry and Remote Sensing*, 80(0):21 – 38, 2013.

[2] S. M. Adler-Golden, M. W. Matthew, G. P. Anderson, G. W. Felde, and J. A. Gardner. Algorithm for de-shadowing spectral imagery. In *International Symposium on Optical Science and Technology*, pages 203–210. International Society for Optics and Photonics, 2002.

[3] Y. Aksoy and A. Aydın Alatan. Utilization of false color images in shadow detection. In A. Fusiello, V. Murino, and R. Cucchiara, editors, *Computer Vision ECCV 2012. Workshops and Demonstrations*, volume 7584 of *Lecture Notes in Computer Science*, pages 472–481. Springer Berlin Heidelberg, 2012.

[4] V. Arévalo, J. González, and G. Ambrosio. Shadow detection in colour high-resolution satellite images. *International Journal of Remote Sensing*, 29(7):1945–1963, 2008.

[5] M. Bevis, S. Businger, T. HERRING, C. Rocken, R. ANTHES, and R. WARE. Gps meteorology- remote sensing of atmospheric water vapor using the global positioning system. *Journal of Geophysical Research*, 97(D14):15787–15801, 1992.

[6] Brad Smith. Illustration of the phong reflection model Wikipedia, the free encyclopedia, 2006. [Online; accessed 16-August-2015].

[7] D. Cai, M. Li, Z. Bao, Z. Chen, W. Wei, and H. Zhang. Study on shadow detection method on high resolution remote sensing image based on his space transformation and ndvi index. In *Geoinformatics, 2010 18th International Conference on*, pages 1–4. IEEE, 2010.

[8] D. Chai and K. N. Ngan. Face segmentation using skin-color map in videophone applications. *Circuits and Systems for Video Technology, IEEE Transactions on*, 9(4):551–564, 1999.

[9] S. Chen, S. Zeng, and C. Xie. Remote sensing and gis for urban growth analysis in china. *Photogrammetric Engineering and Remote Sensing*, 66(5):593–598, 2000.

[10] Y. Chen, D. Wen, L. Jing, and P. Shi. Shadow information recovery in urban areas from very high resolution satellite imagery. *International Journal of Remote Sensing*, 28(15):3249–3254, 2007.

[11] K.-L. Chung, Y.-R. Lin, and Y.-H. Huang. Efficient shadow detection of color aerial images based on successive thresholding scheme. *Geoscience and Remote Sensing, IEEE Transactions on*, 47(2):671–682, 2009.

[12] J. Coakley. Reflectance and albedo, surface. *Encyclopedia of the Atmosphere, JR Holton and JA Curry, eds.(Academic, 2003)*, pages 1914–1923, 2003.

[13] P. M. Dare. Shadow analysis in high-resolution satellite imagery of urban areas. *Photogrammetric Engineering & Remote Sensing*, 71(2):169–177, 2005.

[14] A. David and P. Jean. Computer vision: a modern approach, 2002.

[15] M. T. Eismann and R. C. Hardie. Hyperspectral resolution enhancement using high-resolution multispectral imagery with arbitrary response functions. *Geoscience and Remote Sensing, IEEE Transactions on*, 43(3):455–465, 2005.

[16] A. Elsharkawy et al. A modified parallelepiped-like method for supervised classification for high resolution satellite imagery. In *CGU Annual Scientific Meeting, Banff, Calgary*, 2011.

[17] C. Ferencz, P. Bognar, J. Lichtenberger, D. Hamar, G. Tarcsai†, G. Timar, G. Molnar, S. Pásztor, P. Steinbach, B. Szekely, et al. Crop yield estimation by satellite remote sensing. *International Journal of Remote Sensing*, 25(20):4113–4149, 2004.

[18] C. Fredembach and S. Süsstrunk. Automatic and accurate shadow detection from (potentially) a single image using near-infrared information. Technical report, 2010.

[19] G. Funka-Lea and R. Bajcsy. Combining color and geometry for the active, visual recognition of shadows. In *Computer Vision, 1995. Proceedings., Fifth International Conference on*, pages 203–209, Jun 1995.

[20] T. Gevers and A. W. Smeulders. Color-based object recognition. *Pattern Recognition*, 32(3):453 – 464, 1999.

[21] M. Golchin, F. Khalid, L. N. Abdullah, and S. H. Davarpanah. Shadow detection using color and edge information. *Journal of Computer Science*, 9(11):1575, 2013.

[22] R. Gonzalez and R. Woods. *Digital Image Processing*. Prentice-Hall, Inc., Upper Saddle River, NJ, USA, 3rd edition, 2006.

[23] J. H. Gruninger, A. J. Ratkowski, and M. L. Hoke. The sequential maximum angle convex cone (smacc) endmember model. In *Defense and Security*, pages 1–14. International Society for Optics and Photonics, 2004.

[24] G. E. Hill and K. J. McGraw. *Bird coloration: function and evolution*, volume 2. Harvard University Press, 2006.

[25] J. Huang, W. Xie, and L. Tang. Detection of and compensation for shadows in colored urban aerial images. In *Intelligent Control and Automation, 2004. WCICA 2004. Fifth World Congress on*, volume 4, pages 3098–3100 Vol.4, June 2004.

[26] R. D. Hudson Jr and J. W. Hudson. The military applications of remote sensing by infrared. *Proceedings of the IEEE*, 63(1):104–128, 1975.

[27] S. B. Idso, R. D. Jackson, and R. J. Reginato. Remote-sensing of crop yields. *Science*, 196(4285):19–25, 1977.

[28] M. K. Jat, P. K. Garg, and D. Khare. Monitoring and modelling of urban sprawl using remote sensing and gis techniques. *International journal of Applied earth Observation and Geoinformation*, 10(1):26–43, 2008.

[29] N. Kerle and C. Oppenheimer. Satellite remote sensing as a tool in lahar disaster management. *Disasters*, 26(2):140–160, 2002.

[30] M. S. Kiver. *Color television fundamentals*. McGraw-Hill, 1955.

[31] R. Kuhne. Potential of remote sensing for traffic applications. In *Intelligent Transportation Systems, 2003. Proceedings. 2003 IEEE*, volume 1, pages 745–749 vol.1, Oct 2003.

[32] Y. Li, P. Gong, and T. Sasagawa. Integrated shadow removal based on photogrammetry and image analysis. *International Journal of Remote Sensing*, 26(18):3911–3929, 2005.

[33] T. Nakajima, G. Tao, and Y. Yasuoka. Simulated recovery of information in shadow areas on ikonos image by combing als data. In *Proceeding of Asian Conference on Remote Sensing (ACRS)*, 2002.

[34] Q. M. Nguyen, P. M. Atkinson, and H. G. Lewis. Super-resolution mapping using hopfield neural network with panchromatic imagery. *International journal of remote sensing*, 32(21):6149–6176, 2011.

[35] F. Omruuzun, D. O. Baskurt, H. Daglayan, and Y. Y. Cetin. Shadow removal from vnir hyperspectral remote sensing imagery with endmember signature analysis. In *SPIE Sensing Technology+ Applications*, pages 94821F–94821F. International Society for Optics and Photonics, 2015.

[36] N. Otsu. A threshold selection method from gray-level histograms. *Automatica*, 11(285-296):23–27, 1975.

[37] A. M. Polidorio, F. C. Flores, N. N. Imai, A. M. Tommaselli, and C. Franco. Automatic shadow segmentation in aerial color images. In *Computer Graphics and Image Processing, 2003. SIBGRAPI 2003. XVI Brazilian Symposium on*, pages 270–277. IEEE, 2003.

[38] W. K. Pratt. *Photometry and Colorimetry*, pages 45–88. John Wiley Sons, Inc., 2006.

[39] J. Rau, N.-Y. Chen, and L.-C. Chen. True orthophoto generation of built-up areas using multi-view images. *Photogrammetric Engineering and Remote Sensing*, 68(6):581–588, 2002.

[40] E. Salvador, A. Cavallaro, and T. Ebrahimi. Cast shadow segmentation using invariant color features. *Computer Vision and Image Understanding*, 95(2):238 – 259, 2004.

[41] P. Sarabandi, F. Yamazaki, M. Matsuoka, and A. Kiremidjian. Shadow detection and radiometric restoration in satellite high resolution images. In *IGARSS*, pages 3744–3747, 2004.

[42] D. Stanescu, M. Stratulat, V. Groza, I. Ghergulescu, and D. Borca. Steganography in yuv color space. In *Robotic and Sensors Environments, 2007. ROSE 2007. International Workshop on*, pages 1–4, Oct 2007.

[43] M. Teke, E. Başeski, A. Ö. Ok, B. Yüksel, and Ç. Şenaras. Multi-spectral false color shadow detection. In *Photogrammetric Image Analysis*, pages 109–119. Springer, 2011.

[44] D. M. Tralli, R. G. Blom, V. Zlotnicki, A. Donnellan, and D. L. Evans. Satellite remote sensing of earthquake, volcano, flood, landslide and coastal inundation hazards. *ISPRS Journal of Photogrammetry and Remote Sensing*, 59(4):185–198, 2005.

[45] V. J. Tsai. A comparative study on shadow compensation of color aerial images in invariant color models. *Geoscience and Remote Sensing, IEEE Transactions on*, 44(6):1661–1671, 2006.

[46] A. Villa, J. Chanussot, J. A. Benediktsson, and C. Jutten. Spectral unmixing for the classification of hyperspectral images at a finer spatial resolution. *Selected Topics in Signal Processing, IEEE Journal of*, 5(3):521–533, 2011.

[47] V. U. Zavorotny and A. G. Voronovich. Scattering of gps signals from the ocean with wind remote sensing application. *Geoscience and Remote Sensing, IEEE Transactions on*, 38(2):951–964, 2000.

[48] Q. Zhan, W. Shi, and Y. Xiao. Quantitative analysis of shadow effects in high-resolution images of urban areas. *International Archives of Photogrammetry and Remote Sensing*, 36(8/W27), 2005.

APPENDIX A

APPENDIX A: SHADOW DETECTION RESULTS

Figure A.1: RGB of images

Figure A.2: Ratio based on saturation and intensity on true color image

Figure A.3: Ratio based on saturation and intensity on false color image

Figure A.4: Ratio based on hue and intensity on true color image

Figure A.5: Ratio based on hue and intensity on false color image

Figure A.6: Ratio based on HCV color space on true color image

Figure A.7: Ratio based on HCV color space on false color image

Figure A.8: Ratio based on $C_1C_2C_3$ color space on true color image

Figure A.9: Ratio based on $C_1C_2C_3$ color space on false color image

Figure A.10: Ratio based on YUV color space on true color image

Figure A.11: Ratio based on YUV color space on false color image

Figure A.12: Ratio based on YC_bC_r color space on true color image

Figure A.13: Ratio based on YC_bC_r color space on false color image

Figure A.14: Ratio based on YIQ color space on true color image

Figure A.15: Ratio based on YIQ color space on false color image

Figure A.16: RGB of images

Figure A.17: Ratio based on saturation and intensity on true color image

Figure A.18: Ratio based on saturation and intensity on false color image

Figure A.19: Ratio based on hue and intensity on true color image

Figure A.20: Ratio based on hue and intensity on false color image

Figure A.21: Ratio based on HCV color space on true color image

Figure A.22: Ratio based on HCV color space on false color image

Figure A.23: Ratio based on $C_1C_2C_3$ color space on true color image

Figure A.24: Ratio based on $C_1C_2C_3$ color space on false color image

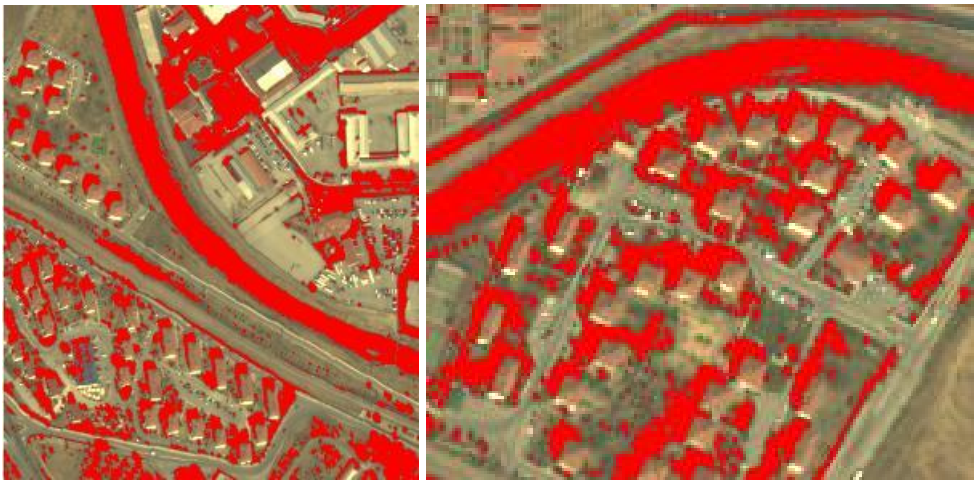

Figure A.25: Ratio based on YUV color space on true color image

Figure A.26: Ratio based on YUV color space on false color image

Figure A.27: Ratio based on YC_bC_r color space on true color image

Figure A.28: Ratio based on YC_bC_r color space on false color image

Figure A.29: Ratio based on YIQ color space on true color image

Figure A.30: Ratio based on YIQ color space on false color image